

Complex nonlinear dynamics of a multidirectional energy harvester with hybrid transduction

Luã G Costa  and Marcelo A Savi* 

Universidade Federal do Rio de Janeiro, COPPE—Mechanical Engineering, Center for Nonlinear Mechanics, 21941-914 Rio de Janeiro, RJ, Brazil

E-mail: savi@mecanica.coppe.ufrj.br and guedes@mecanica.coppe.ufrj.br

Received 27 May 2024, revised 25 August 2024

Accepted for publication 18 September 2024

Published 4 October 2024



Abstract

Mechanical energy harvesting has increasing scientific and technological interests due to novel energetic challenges. A critical issue in classical cantilever-based mechanical energy harvesting systems is the lack of multidirectional energy conversion capabilities and, due to that, deviations from the excitation source can drastically reduce their performance. This limitation has led to the development of energy harvesters with attached pendula, serving as a direction coupling mechanism. Nevertheless, the pendulum structure itself can act as an energy absorber, drastically reducing the harvester performance in certain scenarios. In order to overcome this issue, a hybrid multidirectional pendulum-based energy harvester has been introduced by the authors. The hybrid transduction integrates a piezoelectric element to capture energy from the principal direction and an electromagnetic transducer to harness rotational energy from the pendulum. This paper presents an in-depth analysis of the hybrid multidirectional pendulum-based energy harvester using a nonlinear dynamics perspective to evaluate the energy harvesting performance. A reduced-order model is proposed to represent the essential characteristics of such systems. A parametric analysis using a nonlinear dynamics perspective is carried out to map the system dynamics and performance. The emergence of complex and rich dynamics is observed, including chaos and hyperchaos. Results reveal the most and least effective combinations of structural parameters in terms of energy conversion. Additionally, the dynamical responses and patterns associated with high performance are identified. These responses are often characterized by a blend of irregular complex behaviors, coupled with a mix of oscillatory and rotational patterns of motion, resulting in wider bandwidth systems.

Supplementary material for this article is available [online](#)

Keywords: multidirectional energy harvesting, hybrid energy harvesting, piezoelectric materials, nonlinear dynamics, chaos, pendulum, electromechanical systems

1. Introduction

Mechanical energy harvesting using smart materials and structures is an emergent technology that has gained significant

attention from researchers since the work done by Williams and Yates (1996). In this regard, the continuous improvements in the semiconductor technology of the 4.0 industry are facilitating the decrease in energy usage in electronic systems (Zhu *et al* 2020). This reduction is enabling the usage of environmental mechanical energy sources such as sound, vibration, tidal, sea waves, wind, and biomechanical motion, as a viable

* Author to whom any correspondence should be addressed.

alternative to enhance the autonomy of electronic devices, with the potential to fully replace the battery in some cases (Toprak and Tigli 2014, Sebald *et al* 2023).

Autonomous wireless sensors, internet of things, and micro- and nano-electromechanical systems are just a few of the fields in which mechanical energy harvesting technology finds broad applications (Dutoit *et al* 2005, Izadgoshasb 2021). Large-scale systems also appear as a potential field of application (Zuo and Tang 2013). Numerous studies regarding capturing energy from civil infrastructure are reported. Erturk (2011) and Peigney and Siegert (2013) have demonstrated the potential of energy harvesting from traffic-induced vibrations. Elhalwagy *et al* (2017) and Wang *et al* (2018) have shown the energy conversion from the small deformation of compressive loading on pavements and buildings. The biomedical field is also targeted as a promising field of application. Deterre *et al* (2012) and Dagdeviren *et al* (2014) showed the usage of flexible energy harvesters to power implantable medical devices, by harnessing energy from the biomechanical motion of internal organs such as lungs, heart, and diaphragm. Wildlife monitoring is also reported in the biomedical field (Li *et al* 2022). Furthermore, the powering of wearable devices by the conversion of biomechanical motion energy (Delnavaz and Voix 2014, Zhao *et al* 2019, Liu *et al* 2021), offshore applications for tidal and wave energy harvesting (Nabavi *et al* 2018), and health monitoring of vehicle parts are also reported applications (Lee and Choi 2014, Tavares and Ruderman 2020).

To convert the mechanical energy into electrical energy, transduction mechanisms are utilized. Electromagnetic transduction is the classical electromechanical conversion mechanism. Its working mechanism is based on the principle of electromagnetic induction, where a current is induced in a conductor when a magnetic flux around the conductor changes. This type of transduction mechanism is commonly used in large-scale robust applications but can be used in microenvironments as well (Cepnik *et al* 2013). In contrast, other physical phenomena, such as triboelectricity and piezoelectricity were also exploited in the last decades to serve as energy conversion mechanisms. Triboelectric-based harvesters use friction between two different material surfaces to create an electric potential between them, which makes these structures adequate for nano to microscale applications (Haroun *et al* 2022). Piezoelectric materials belong to a class of smart materials that convert mechanical stimuli into electrical signals. This reversible process is denominated the direct piezoelectric effect, which generates an electrical charge proportional to the mechanical force/pressure applied. Piezoelectric transducers can be utilized in micro to large-scale environments (Clementi *et al* 2022). Magnetostrictive (Deng and Dapino 2017) and flexoelectric (Tripathy *et al* 2021) are other types of transduction mechanisms that also have been reported in the literature.

Each type of transduction mechanism has its advantages and disadvantages. To counteract the disadvantages, the combination of different transduction mechanisms into a single energy harvesting device allows the exploitation of the unique advantages of each transducer, resulting in an enhanced energy

harvesting capacity. Zhong *et al* (2015) reported the combination of both electromagnetic and triboelectric transducers to design a hybrid rotational harvester focused on scavenging biomechanical energy, using it as a mobile power source. Wang *et al* (2023) proposed a new speed-amplified tri-hybrid energy harvester utilizing piezoelectric, triboelectric, and electromagnetic transducers to harness structural and biomechanical vibration energy. Additionally, Chung *et al* (2021) proposed a Kresling origami design that exploits both piezoelectric and triboelectric elements to harvest the energy dissipated by contact strain, and another triboelectric element in slide mode to take advantage of the resulting rotational motion due to origami folding. Egbe *et al* (2022) also employed three distinct transduction elements to increase the performance of a rotational wind energy harvester device to power local sensors. Furthermore, other authors also show the performance improvement due to the employment of hybrid conversion strategies (Halim *et al* 2019, Yang and Cao 2019, Gao *et al* 2020, Xiao *et al* 2022, Bai *et al* 2024), highlighting the potential of hybrid transduction in enhancing energy harvesting performance.

Energy harvesters usually operate as resonators, such as structural elements like beams and plates. In this regard, when operating in a linear regime, their good performance is related to the resonant conditions, limited to frequencies close to the structure's natural frequencies. The addition of nonlinear modulations proved to be an effective solution for increasing their operation bandwidth and, in some cases, the maximum output power, when subjected to environmental uncertainties. Multistable systems promoted by either magnetic interactions or buckling appear as one of the most common nonlinear modifications (Masana and Daqaq 2010, De Paula *et al* 2015). Multistable harvesters present a high level of enhanced performance showing increases in both output power and bandwidth. These systems are known for their characteristic potential energies that are formed by peaks and valleys of energy. The drawback of multistable harvesters is related to situations where available environmental energy is not enough to overcome energetic barriers defined by potential energy peaks. In these scenarios, the harvester dynamics stays trapped around an energy valley, drastically reducing its performance (Stanton *et al* 2009).

Nonsmoothness is another kind of nonlinearity incorporated into the design of energy harvesting systems to enhance performance. This modulation enhances the operation bandwidth, at the cost of the reduction of the maximum output power (Liu *et al* 2012, Zhou *et al* 2015, Ai *et al* 2019). This type of modulation is useful when dealing with applications where the available mechanical energy presents a wide range of frequencies. Nevertheless, successive impacts can cause mechanical wear over time, which is a disadvantage of this kind of system. Additionally, adaptive systems are also reported. Adeodato *et al* (2021) and Yuan *et al* (2019) have demonstrated the synergistic use of smart materials combining piezoelectric and shape memory materials to actively control the natural frequency of the harvester, enabling

enhanced performance at different excitation frequencies. Adaptive multistable systems with variable magnet positions have also demonstrated that the energy harvesting performance can be drastically enhanced by a small external intervention (Savi and Savi 2024).

Quasi-zero stiffness modulations are also beneficial to enhance energy harvesting capacity. Margielewicz *et al* (2022) proposed a modification of the cantilever design by adding a set of springs specially configured, resulting in a quasi-flat potential energy. They showed that this type of harvester can be better than the tristable harvester, especially at low excitation amplitudes. The drawback of this kind of system is the robustness of the set of springs, which can limit applications in small-scale environments.

The literature also reports the design of alternative structures different from the traditional cantilever-based structure. Yang *et al* (2017) suggested the incorporation of an arc-shaped segment into the cantilever design, which enhanced the maximum output power. Following this, bistable harvesters were reported that leveraged this characteristic (Zhang *et al* 2018, Chen *et al* 2021a, 2021b). Additionally, multimodal structures have been proposed. Caetano and Savi (2021) proposed a pizza-shaped energy harvester with irregular slices demonstrating a significantly expanded bandwidth compared to the conventional cantilever harvester. Wu *et al* (2013) proposed a cutout structure featuring an inner and outer beam. This design brought the natural frequencies of the system close together, concentrating the regions of high performance within a specific frequency range, thereby expanding its bandwidth. Wu *et al* (2014) later improved the cutout configuration by introducing bistable properties through the addition of a magnetic interaction attached to the inner beam. Subsequently, Costa and Savi (2024a) and Costa *et al* (2024) proposed an enhanced multistable version of the inner–outer harvester, specifically designed for applications in compact and limited spaces. A space-efficient design was considered by incorporating more transducers into key regions of the structure. The multistability resulting from the use of two sets of magnets, one attached to the inner beam and the other attached to the outer beam, defines complex nonlinear dynamics that can be properly exploited.

Although numerous enhancements to the cantilever design have been developed to date, the capability for multidirectional energy harvesting remains a challenge that needs to be properly addressed. In this context, bending-torsional modes of operation have been extensively explored through the use of asymmetric structures (Abdelkefi *et al* 2011, Abdelmoula *et al* 2017, Gao *et al* 2017, Jia *et al* 2020, Li *et al* 2020, Wang *et al* 2022a) and twisting phenomena (Hu *et al* 2020). Additionally, rotational support mechanisms for autonomous omnidirectional energy harvesting (Wang *et al* 2022b), as well as devices comprising beams oriented in different directions (Su and Zu 2013, Fan *et al* 2014), have also been investigated. Moreover, pendulum structures are an interesting and effective solution for achieving multidirectionality (Wu *et al* 2018, Kumar *et al* 2019, Malaji *et al* 2020). Multidirectional coupling is intrinsic

to pendulum devices (Chen *et al* 2022, Wang 2023), which can be integrated into the cantilever design to introduce multidirectional characteristics, preserving its original size (Xu and Tang 2015, Pan *et al* 2019, 2021, Wu *et al* 2022). Nevertheless, the introduction of a pendulum to the system can result in scenarios where the pendulum acts as an energy absorber, compromising energy harvesting. Costa and Savi (2024b) demonstrated that such scenarios occur frequently, thereby reducing the overall energy harvesting capacity.

On this basis, it is evident that the introduction of nonlinearities is the essential approach for enhancing energy harvesting capacity. In this regard, the dynamics of the nonlinear energy harvesting systems are directly interconnected with their overall performance. In general, energy harvesting systems present complex nonlinear dynamics and a proper performance analysis must be guided by a nonlinear dynamics perspective (Costa *et al* 2021). The manifestation of different types of dynamical responses (Cabeza *et al* 2013) and the emergence of multiple solutions (Margielewicz *et al* 2023) are some aspects of dynamical complexity. This intrinsic complexity needs to be analyzed by proper tools (Costa *et al* 2021, Reis and Savi 2022).

This work deals with the hybrid multidirectional energy harvester (HMEH) proposed in a previous work (Costa and Savi 2024b). The design is composed of a piezoelectric cantilever-based energy harvester with an attached pendulum associated with an electromagnetic rotational energy converter. The harvester is developed in such a way that the system can perform multidirectional energy harvesting, mitigating the energy-absorbing effects of the pendulum, and increasing the performance and overall bandwidth of the system. Hybrid transduction allows one to convert mechanical energy from the piezoelectric element and also from an electromagnetic device incorporated at the base of the pendulum, harvesting the energy that would otherwise be lost. A reduced-order model is presented to represent the key parameters of this type of harvester. This investigation extends the previous work by conducting a detailed parametric analysis from a nonlinear dynamics perspective, aiming to further map and characterize the system's performance and dynamical behavior. Results show complex responses including chaos and hyperchaos, which points to the need for a deep dynamical investigation to properly design the energy harvesting system.

After this introduction, this work is organized as follows: section 2 establishes the conceptual representation of the HMEH, depicting the evolution from the classical piezoelectric energy harvester (CPEH) to the proposed multidirectional hybrid energy harvester. A theoretical model is developed to describe the qualitative characteristics of the structure. Section 3 presents an extensive numerical analysis based on a nonlinear dynamics perspective aiming to map and quantify different structural and dynamical characteristics of the HMEH, associating these characteristics with the harvester's performance level. Finally, the conclusions are presented in section 4, and an appendix is provided to elucidate some methodologies regarding the analyses.

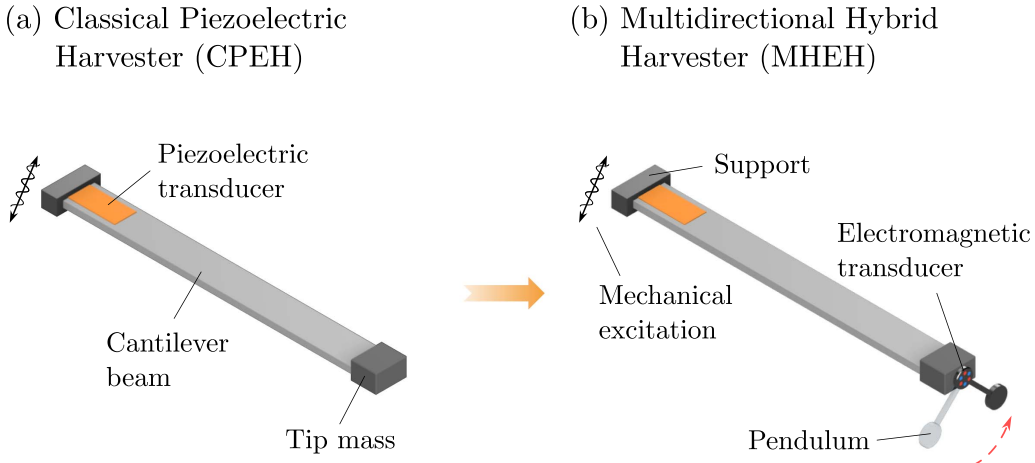


Figure 1. Conceptual representation of depicting the evolution of (a) the classical piezoelectric energy harvester (CPEH), composed by a piezoelectric transducer and a cantilever beam structure with a tip mass, (b) to the multidirectional hybrid energy harvester (MHEH), composed by the CPEH plus the addition of a pendulum structure with an electromagnetic transducer at the pendulum's support.

2. Design and theoretical model

Consider the conceptual representation of the evolution of the CPEH to the HMEH as depicted in figure 1. The CPEH is composed of a structural cantilever beam element embedded in a rigid support. A piezoelectric transducer is attached to the superior surface of the beam, while a tip mass element is added to its free end, as presented in figure 1(a). The MHEH design incorporates a pendulum structure with an additional electromagnetic transducer at the pendulum's support in order to harness its rotational energy (figure 1(b)). This layout employs the pendulum as a coupling mechanism between directions to diffuse energy in multiple directions.

2.1. Physical modeling

The design of the harvesters presented in figure 1 can be represented by a general lumped model displayed in figure 2. It considers both structural beam and its tip mass as a lumped mass of effective mass m_s , where the tip mass is considered to be significantly heavier than the beam's mass. Also, a pendulum element of length L_p and effective mass m_p attached to the structure. The effects of gravity, g , are considered, and the equivalent stiffness and damping coefficients are represented by k_i ($i = x, z, pz$) and c_j ($j = x, z, em, p$), where subscripts x and z refer to the plane directions, while subscript p is used to represent pendulum characteristics; subscripts pz and em refer to the piezoelectric and electromagnetic transducers, respectively.

The piezoelectric transducer is attached to the z -direction, to represent the piezoelectric element attached to the top surface structure, while the electromagnetic transducer is attached to the support of the pendulum. Each transducer can be represented by equivalent circuits, where the coupling between the electrical to the mechanical domain is represented by a unique electromechanical coupling term. The piezoelectric element is associated with a circuit represented in figure 2(b), and

the coupling term is related to the current source by a linear relationship of $I_{pz}(t) = \theta_{pz}\dot{z}(t)$. The current source is connected in parallel to an equivalent internal capacitance, C_{pz} , an internal resistance, R_{ipz} , and an external resistance R_{lpz} . Conversely, the electromagnetic transducer is represented by figure 2(c), where the electromechanical coupling of the electromagnetic transducer is associated with a voltage source by a linear relationship of $v_{em}(t) = \theta_{em}\dot{\phi}(t)$. This source is connected in series to an equivalent inductance, L_{em} , an internal resistance, R_{iem} , and an external load resistance, R_{lem} . The equivalent resistance of the piezoelectric circuit is represented by $R_{pz} = R_{ipz}R_{lpz}/(R_{lpz} + R_{ipz})$, while the equivalent resistance of the electromagnetic circuit is represented by $R_{em} = R_{iem} + R_{lem}$.

The system is subjected to a multidirectional support excitation of $\mathbf{r}_b(t) = r_b(t)[\sin(\mu)\hat{\mathbf{e}}_x + \cos(\mu)\hat{\mathbf{e}}_z]$, where the bold notation refers to vectors and italic notation refers to scalars; μ is the angle between the external excitation vector, $\mathbf{r}_b(t)$, and the z -direction. $r_b(t)$ is the excitation function. The vectors $\hat{\mathbf{e}}_x$ and $\hat{\mathbf{e}}_z$ are the base vectors of each Cartesian direction, x and z , respectively. This way, the support excitations in the horizontal and vertical directions are described by $x_b(t) = r_b(t)\sin(\mu)$ and $z_b(t) = r_b(t)\cos(\mu)$, respectively.

The modeling considers the absolute structure position,

$$\begin{aligned} \mathbf{r}_s(t) &= [x_b(t) + x_s(t)]\hat{\mathbf{e}}_x + [z_b(t) + z_s(t)]\hat{\mathbf{e}}_z \\ &= [x_b(t) + x(t)]\hat{\mathbf{e}}_x + [z_b(t) + z(t) + z_{st}]\hat{\mathbf{e}}_z, \end{aligned} \quad (1)$$

where $x(t)$ and $z(t)$ are the positions of mass relative to the base, and $z_{st} = (m_s + m_p)g/(k_z + k_{pz})$ is the static deflection of the structure due to gravity action. On the other hand, the absolute position of the pendulum is given by

$$\begin{aligned} \mathbf{r}_p(t) &= [x_b(t) + x(t) + x_p(t)]\hat{\mathbf{e}}_x \\ &\quad + [z_b(t) + z(t) + z_{st} + z_p(t)]\hat{\mathbf{e}}_z \\ &= [x_b(t) + x(t) + L_p \sin(\phi(t))]\hat{\mathbf{e}}_x \\ &\quad + [z_b(t) + z(t) + z_{st} + L_p \cos(\phi(t))]\hat{\mathbf{e}}_z, \end{aligned} \quad (2)$$

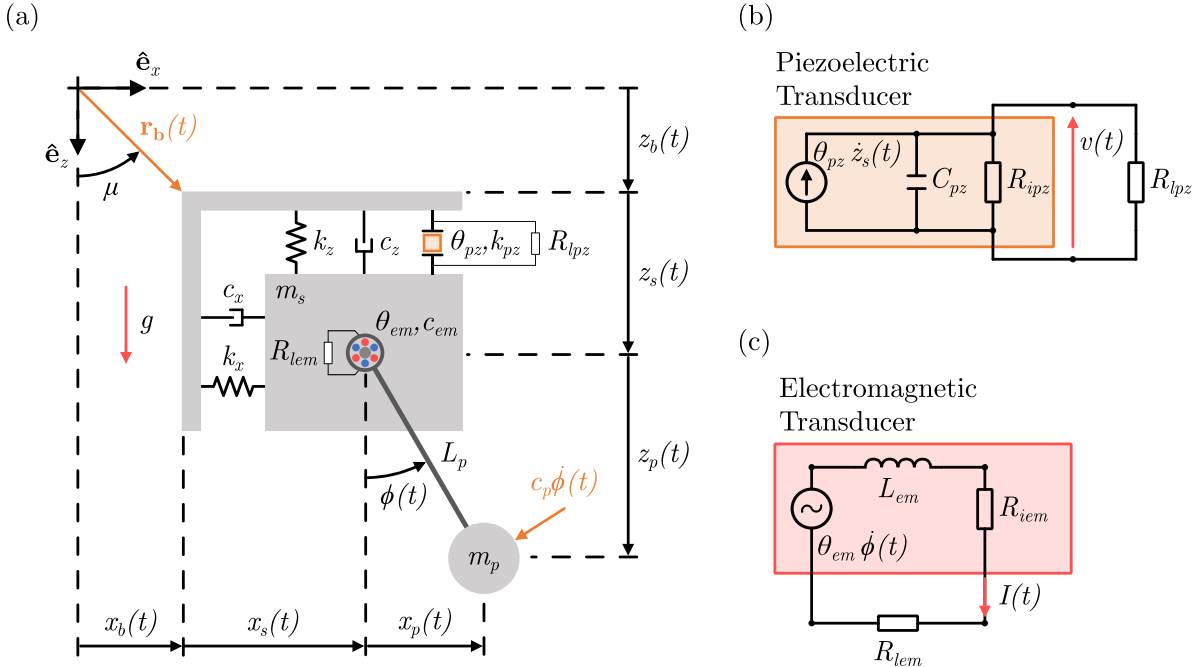


Figure 2. (a) General lumped model representing the Hybrid Multidirectional Energy Harvester (HMEH). (b) The equivalent circuit of the piezoelectric transducer is attached to an external resistance. (c) The equivalent circuit of the electromagnetic transducer is attached to an external resistance.

where $\phi(t)$ represents the angular displacement of the pendulum relative to the vertical z axis.

An energetic approach is of concern and therefore, a Lagrangian is defined as $\mathcal{L} = T - U + W$, considering five generalized coordinates (three mechanical and two electrical), $\mathbf{Q} = [x(t), z(t), \phi(t), \psi(t), q(t)]$. Here $\psi(t)$ represents the flux linkage of the piezoelectric circuit, and $q(t)$ denotes the electric charge in the electromagnetic circuit. This formulation leads to the following electromechanical Euler–Lagrange equation,

$$\frac{d}{dt} \left(\frac{\partial \mathcal{L}}{\partial \dot{Q}_i} \right) - \frac{\partial \mathcal{L}}{\partial Q_i} + \frac{\partial D}{\partial \dot{Q}_i} = 0. \quad (3)$$

On this basis, the system energy needs to be evaluated. The total kinetic energy is the composition of the structure and the pendulum kinetic energies,

$$\begin{aligned} T &= T_s + T_p \\ &= \frac{1}{2} m_s \dot{x}_s(t) \cdot \dot{x}_s(t) + \frac{1}{2} m_p \dot{r}_p(t) \cdot \dot{r}_p(t) \\ &= \frac{1}{2} m_p \left\{ [\dot{x}(t) + \dot{x}_b(t) + L_p \dot{\phi}(t) \cos(\phi(t))]^2 \right. \\ &\quad \left. + [\dot{z}(t) + \dot{z}_b(t) - L_p \dot{\phi}(t) \sin(\phi(t))]^2 \right\} \\ &\quad + \frac{1}{2} m_s \left\{ [\dot{x}(t) + \dot{x}_b(t)]^2 + [\dot{z}(t) + \dot{z}_b(t)]^2 \right\}. \end{aligned} \quad (4)$$

Linear constitutive behavior is adopted for structure and piezoelectric elements and therefore, the restitution forces are represented as follows,

$$f_x(t) = -k_x x(t), \quad (5)$$

$$f_z(t) = -k_z z(t), \quad (6)$$

$$f_{pz}(t) = -k_{pz} z(t), \quad (7)$$

On this basis, the total potential energy is written as the sum of the main structure, piezoelectric element, and pendulum potential energies, being given by.

$$\begin{aligned} U &= U_s + U_p \\ &= - \int_0^{x_s(t)} f_x(t) dx - \int_0^{z_s(t)} [f_z(t) + f_{pz}(t)] dz \\ &\quad - \int_0^{z_b(t) + z_s(t)} m_s g dz - \int_0^{z_b(t) + z_s(t) + z_p(t)} m_p g dz \\ &= \frac{1}{2} k_x x(t)^2 + \frac{1}{2} (k_z + k_{pz}) [z(t) + z_{st}]^2 \\ &\quad - m_s g [z_b(t) + z(t) + z_{st}] \\ &\quad - m_p g [z_b(t) + z(t) + z_{st} + L_p \cos(\phi(t))]. \end{aligned} \quad (8)$$

The piezoelectric electromechanical coupling, θ_{pz} , is determined by the properties of the piezoelectric material, its geometry, and dimensions. In contrast, the electromechanical coupling due to the electromagnetic converter, θ_{em} , can be determined by the geometric characteristics of the coil(s), the properties of the magnet(s) within the converter, the intensity of their magnetic field(s) and how these elements are positioned and distributed within the transducer. For the sake of simplicity, the coupling coefficients are assumed to be constants.

The electrical behavior is treated by considering the relation between the flux linkage, $\psi(t)$, and the voltage, $v(t)$, across the piezoelectric circuit as $\psi(t) = v(t)$. Besides, consider the

relation between the charge, $q(t)$, and the current, $I(t)$, flowing in the electromagnetic circuit as $\dot{q}(t) = I(t)$. By assuming that the total energy, W , of the electrical domain can be represented by the sum of the electric energy of the piezoelectric element, W_e , and the magnetic energy of the electromagnetic transducer, W_m , as described by equation (9), where W_C , W_{pz} , W_L and W_{em} are the electric energy in the capacitance, the piezoelectric energy, the magnetic energy in the inductance and the electromagnetic energy, respectively. The details of this formulation can be seen in Preumont (2006).

$$\begin{aligned} W &= W_e + W_m \\ &= W_C + W_{pz} + W_L + W_{em} \\ &= \frac{1}{2} C_{pz} \dot{\psi}(t)^2 + \theta_{pz} \dot{\psi}(t) z(t) + \frac{1}{2} L_{em} \dot{q}(t)^2 + \theta_{em} \dot{q}(t) \phi(t). \end{aligned} \quad (9)$$

The dissipation is expressed in four major sources: viscous damping in the structure, viscous damping external to the pendulum structure, magnetic damping resulting from the interactions between the magnet(s) and coil(s) within the electromagnetic transducer, and electrical resistances within the circuits. These sources can be modeled through dissipation functions (Preumont 2006, Meirovitch 2010), as depicted by equation (10), where D_x and D_z are the dissipation functions associated with the nonconservative viscous force in x and z directions. D_{ϕ_e} is the dissipation function associated with the interaction between the pendulum structure and the surrounding media, while D_{ϕ_i} is the electromechanical dissipation associated with the magnetic forces within the electromagnetic transducer. D_{pz} and D_{em} are the dissipation functions that account for the resistive elements of the circuits.

$$\begin{aligned} D &= D_x + D_z + D_{\phi_e} + D_{\phi_i} + D_{pz} + D_{em} \\ &= \frac{1}{2} c_x \dot{x}(t)^2 + \frac{1}{2} c_z \dot{z}(t)^2 + \frac{1}{2} c_p L_p \dot{\phi}(t)^2 + \frac{1}{2} c_{em} \dot{\phi}(t)^2 \\ &\quad + \frac{1}{2} \frac{\dot{\psi}(t)^2}{R_{pz}} + \frac{1}{2} R_{em} \dot{q}(t)^2. \end{aligned} \quad (10)$$

At this point, it is possible to use the Euler–Lagrange equation (3) to build the electromechanical governing equations where the (t) is suppressed in the notation:

$$\begin{aligned} (m_s + m_p) \ddot{x} + c_x \dot{x} + k_x x + m_p L_p [\ddot{\phi} \cos(\phi) - \dot{\phi}^2 \sin(\phi)] \\ = -(m_s + m_p) \ddot{x}_b; \end{aligned} \quad (11)$$

$$(m_s + m_p) \ddot{z} + c_z \dot{z} + (k_z + k_{pz}) z - \theta_{pz} v \\ - m_p L_p [\ddot{\phi} \sin(\phi) + \dot{\phi}^2 \cos(\phi)] = -(m_s + m_p) \ddot{z}_b; \quad (12)$$

$$\begin{aligned} m_p L_p^2 \ddot{\phi} + (c_{em} + c_p L_p) \dot{\phi} + m_p L_p [\ddot{x} \cos(\phi) \\ + (g - \ddot{z}) \sin(\phi)] - \theta_{em} I = m_p L_p [\ddot{z}_b \sin(\phi) - \ddot{x}_b \cos(\phi)]; \end{aligned} \quad (13)$$

$$C_{pz} \dot{v} + \frac{v}{R_{pz}} + \theta_{pz} \dot{z} = 0; \quad (14)$$

$$L_{em} \dot{I} + R_{em} I + \theta_{em} \dot{\phi} = 0. \quad (15)$$

By assuming a harmonic external forcing of

$$\mathbf{r}_b = x_b \hat{\mathbf{e}}_x + z_b \hat{\mathbf{e}}_z = A \sin(\omega t) [\sin(\mu) \hat{\mathbf{e}}_x + \cos(\mu) \hat{\mathbf{e}}_z]. \quad (16)$$

It results in the following:

$$\ddot{\mathbf{r}}_b = \ddot{x}_b \hat{\mathbf{e}}_x + \ddot{z}_b \hat{\mathbf{e}}_z = -A \omega^2 \sin(\omega t) [\sin(\mu) \hat{\mathbf{e}}_x + \cos(\mu) \hat{\mathbf{e}}_z]. \quad (17)$$

In order to generalize the analysis, normalization is performed by considering a reference length, L , a reference voltage V , and a reference current I , resulting in the dimensionless electromechanical equations given by:

$$\begin{aligned} (1 + \rho) \ddot{x} + 2\zeta_x \dot{x} + \Omega_s^2 x + \rho \ell [\ddot{\phi} \cos(\bar{\phi}) - \dot{\phi}^2 \sin(\bar{\phi})] \\ = -(1 + \rho) \ddot{x}_b; \end{aligned} \quad (18)$$

$$\begin{aligned} (1 + \rho) \ddot{z} + 2\zeta_z \dot{z} + \bar{z} - \chi_{pz} \bar{v} - \rho \ell [\ddot{\phi} \sin(\bar{\phi}) + \dot{\phi}^2 \cos(\bar{\phi})] \\ = -(1 + \rho) \ddot{z}_b; \end{aligned} \quad (19)$$

$$\begin{aligned} \ddot{\phi} + 2\zeta_\phi \dot{\phi} + \Omega_\phi^2 \sin(\bar{\phi}) - \chi_{em} \bar{I} + \frac{1}{\ell} [\ddot{x} \cos(\bar{\phi}) - \ddot{z} \sin(\bar{\phi})] \\ = \frac{1}{\ell} [\ddot{z}_b \sin(\bar{\phi}) - \ddot{x}_b \cos(\bar{\phi})]; \end{aligned} \quad (20)$$

$$\dot{\bar{v}} + \frac{\bar{v}}{\varphi_{pz}} + \kappa_{pz} \dot{\bar{z}} = 0; \quad (21)$$

$$\dot{\bar{I}} + \varphi_{em} \bar{I} + \kappa_{em} \dot{\bar{\phi}} = 0. \quad (22)$$

These equations are related to the dimensionless parameters presented in table 1.

2.2. Performance metrics

The performance of the energy harvesting system is evaluated with the definition of the electrical power associated with both piezoelectric and electromagnetic circuits. The total instantaneous electrical power consists of the sum of the instantaneous electrical power in each individual circuit, as represented by equation (23). Thus, the average electrical power, defined over the interval $t_0 \leq t \leq t_f$, is represented by equation (24), where v^{RMS} and I^{RMS} are the root-mean-square (RMS) of the output voltage of the piezoelectric circuit and the output current of the electromagnetic circuit, respectively, being defined by equation (25).

$$P = P_{pz} + P_{em} = \frac{1}{R_{pz}} v^2 + R_{em} I^2, \quad (23)$$

$$P_{\text{avg}} = \frac{1}{t_f - t_0} \int_{t_0}^{t_f} P dt = \frac{1}{R_{pz}} (v^{\text{RMS}})^2 + R_{em} (I^{\text{RMS}})^2, \quad (24)$$

where the RMS of any quantity can be defined as:

$$\square^{\text{RMS}} = \sqrt{\frac{1}{t_f - t_0} \int_{t_0}^{t_f} [\square(t)]^2 dt}. \quad (25)$$

Table 1. System parameters and values used in the analyses.

Parameter Description	Symbol	Definition	Value
Natural frequency of the main structure in x	ω_x	$\sqrt{k_x/m_s}$	—
Natural frequency of the main structure in z	ω_z	$\sqrt{k_z/m_s}$	—
Linearized natural frequency of the pendulum	ω_ϕ	$\sqrt{g/L_p}$	—
Normalized time	τ	$\omega_z t$	—
Normalized x displacement of the main structure	$\bar{x}(\tau)$	$x(t)/L$	—
Normalized z displacement of the main structure	$\bar{z}(\tau)$	$z(t)/L$	—
Normalized angle of the pendulum structure	$\bar{\phi}(\tau)$	$\phi(t)$	—
Normalized voltage of the piezoelectric circuit	$\bar{v}(\tau)$	$v(t)/V$	—
Normalized current of the electromagnetic circuit	$\bar{I}(\tau)$	$I(t)/\mathcal{I}$	—
Normalized base excitation frequency	Ω	ω/ω_z	0.01 → 2
Normalized base excitation amplitude	γ	A/L	0.01 → 0.5
Normalized angle of the base excitation vector $\mathbf{r}_b(t)$	$\bar{\mu}$	μ	45°
Normalized base excitation displacement in the x -direction	$\bar{x}_b(\tau)$	$\gamma \sin(\Omega\tau) \sin(\bar{\mu})$	—
Normalized base excitation displacement in the z -direction	$\bar{z}_b(\tau)$	$\gamma \sin(\Omega\tau) \cos(\bar{\mu})$	—
Ratio of masses	ρ	m_p/m_s	0.5
Normalized damping coefficient of the main structure in x	ζ_x	$c_x/(2\omega_z m_s)$	0.025
Normalized damping coefficient of the main structure in z	ζ_z	$c_z/(2\omega_z m_s)$	0.025
Normalized total damping coefficient of the pendulum structure	ζ_ϕ	$\frac{[(c_{em}/L_p) + c_p]}{2\omega_z L_p m_s}$	0.0025
Ratio of natural frequencies of the main structure	Ω_s	ω_x/ω_z	0.01 → 2
Ratio of natural frequencies of the pendulum and the z -direction	Ω_ϕ	ω_ϕ/ω_z	0.01 → 2
Normalized pendulum length	ℓ	L_p/L	1
Normalized piezoelectric coupling in the mechanical ODE	χ_{pz}	$\theta_{pz} V/(k_z L)$	0.05
Normalized electromagnetic coupling in the mechanical ODE	χ_{em}	$\theta_{em} \mathcal{I}/(\rho k_z L_p^2)$	0.04
Normalized piezoelectric coupling in the piezo circuit ODE	κ_{pz}	$\theta_{pz} L/(C_{pz} V)$	0.5
Normalized EM coupling in the electromagnetic circuit ODE	κ_{em}	$\theta_{em}/(L_{em} \mathcal{I})$	0.4
Normalized equivalent resistance of the piezoelectric circuit	φ_{pz}	$C_{pz} R_{pz} \omega_z$	1
Normalized equivalent resistance of the electromagnetic circuit	φ_{em}	$R_{em}/(L_{em} \omega_z)$	0.25
Normalized electrical output power of the piezoelectric circuit	$P_{pz}(\tau)$	$P_{pz}(t)/(C_{pz} \omega_z V^2)$	—
Normalized electrical output power of the electromagnetic circuit	$P_{em}(\tau)$	$P_{em}(t)/(L_{em} \omega_z \mathcal{I}^2)$	—

Furthermore, based on these concepts and according to table 1, the normalized average electrical output power can be determined by,

$$\bar{P}_{\text{avg}} = \bar{P}_{pz} + \bar{P}_{em} = \frac{1}{\varphi_{pz}} (\bar{v}^{\text{RMS}})^2 + \varphi_{em} (\bar{I}^{\text{RMS}})^2. \quad (26)$$

3. Dynamics and performance

This section presents a parametric analysis considering four key parameters: the ratio between natural frequencies of the main structure, Ω_s ; the ratio between natural frequencies of the pendulum and the structure's z -direction, Ω_ϕ ; the normalized excitation amplitude, γ ; and the normalized excitation frequency, Ω . The main objective of the analysis is to identify the best and the worst combinations of Ω_s and Ω_ϕ parameters in terms of overall performance by considering a wide range of excitation parameters, γ and Ω . Besides, the angle of base excitation, $\bar{\mu}$, is maintained at 45° in order to subject the system to a symmetric multidirectional excitation of which the magnitude components of each direction, z and x , are equal. The electrical parameters are based on the literature (Erturk and Inman 2011, De Paula *et al* 2015, Costa and Savi

2024b), and the remaining constant parameter values are listed in table 1.

The parametric analysis is based on a nonlinear dynamics perspective framework employing five types of diagrams: the Dynamical Responses Diagrams (DRDs), the Lyapunov Exponents Diagrams (LEDs), the Average Output Power Diagrams (OPDs), the Occurrence Diagrams (OCDs), and the Dynamical Pattern Diagrams (DPDs). Each diagram shows an important characteristic of the HMEH in a two-dimensional parameter space of choice in order to characterize the system's dynamics and performance with robustness. Different excitation parameters are of concern.

These diagrams are built with a grid of $N_x \times N_y$ sample points within a two-dimensional parameter space of choice. Each point of the diagram is related to a time series from the integration of the governing equations from an initial time, τ_0 , to a final time, τ_f , considering a suitable integration time step, $\Delta\tau = 2\pi/(\Omega N)$, with $N = 6000$ determined by a convergence analysis. A specific point in time, $\tau_{\text{trans}} = 0.8125\tau_f$, is chosen to define the beginning of the steady-state response. All sample points have the same initial condition of $\bar{x}(0) = \dot{\bar{x}}(0) = \ddot{\bar{x}}(0) = \bar{\phi}(0) = \dot{\bar{\phi}}(0) = \ddot{\bar{\phi}}(0) = \bar{v}(0) = \dot{\bar{v}}(0) = \ddot{\bar{v}}(0) = \bar{I}(0) = 0$ to standardize the analyses.

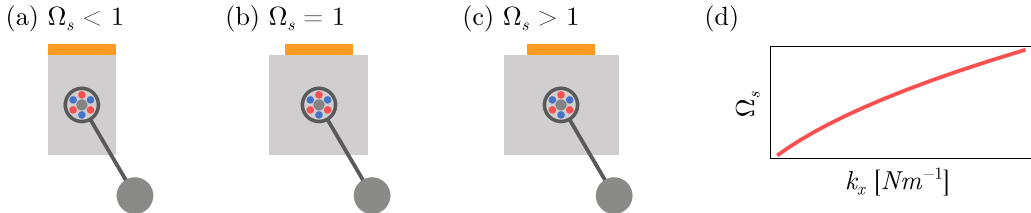


Figure 3. Illustrative representation of the ratio of natural frequencies, Ω_s . (a) $\Omega_s < 1$ indicates that the x -direction is softer than the z -direction, depicted by a shorter beam width in the x -direction. (b) $\Omega_s = 1$ signifies equal stiffness in both x and z directions, represented by identical beam widths in both directions. (c) $\Omega_s > 1$ showcases a stiffer x -direction compared to the z -direction, depicted by a wider beam width in the x -direction. (d) Changes in Ω_s as the stiffness in x -direction, k_x , increases.

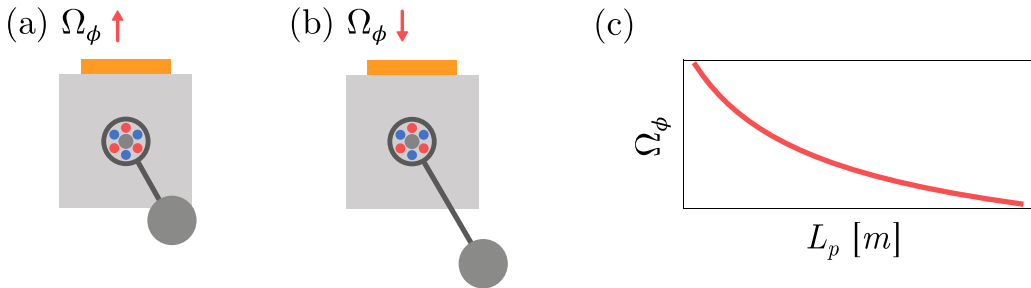


Figure 4. Illustrative representation of the ratio of natural frequencies of the pendulum and the z direction, Ω_ϕ . (a) Representation of a higher Ω_ϕ , corresponding to a shorter pendulum length. (b) Representation of a lower Ω_ϕ , indicating a wider pendulum length. (c) Change in Ω_ϕ as the pendulum length, L_p , increases.

3.1. HMEH key characteristics

Initially, it is important to contextualize the parameters and their influence on the dynamical behavior and harvester performance. Mechanical available ambient energy constitutes input parameters, γ —the normalized magnitude of excitation and Ω —the normalized excitation frequency. Note that $\Omega = 1$ means that the excitation frequency matches the beam's natural frequency in the z -direction. On the other hand, Ω_s is the ratio between the natural frequency of the beam's x -direction and z -direction; Ω_ϕ is the ratio between the linearized natural frequency of the pendulum and the beam's natural frequency in z -direction. Note that $\Omega_s = 1$ means that the natural frequencies of the beam structure are the same in x and z directions; $\Omega_s > 1$ means that the x -direction is stiffer than the z -direction. This characteristic is illustrated in figure 3, where a simplified frontal view of the HMEH beam structure is depicted. Furthermore, figure 4 represents the meaning of Ω_ϕ parameter, which is closely related to the pendulum's length, L_p . A higher value of Ω_ϕ means a shorter pendulum length.

3.2. Dynamical responses

This subsection presents a discussion about the distinct dynamical responses of the HMEH. Diagrams are built assuming constant values of excitation parameters γ and Ω , employing a grid of 500×500 sample points within the $\Omega_s \times \Omega_\phi$ parameter space, each from 0.01 to 2.

Figure 5 shows the DRD, LEDs and OPDs for excitation parameters $\gamma = 0.1$ and $\Omega = 1.2$. Figure 5(a) displays the

DRD, where different steady-state dynamical behaviors are classified for each time series sample. Different periodicities are classified by different colors, considering that T represents the excitation period: dark gray (1T), yellow (2T), light green (3T), orange (4T), and purple (5T). Light blue is employed to represent responses from a period equal to or greater than 6T, to quasi-periodic, labeled as multiple periods (MP). Red regions represent chaotic (CH) responses, while dark red regions represent hyperchaotic (HC) responses. The detailed classification procedure is comprehensively explained in appendix A.1.

LEDs are presented in figures 5(c) and (d), being complementary diagrams to the DRD that show the value of each of the two largest Lyapunov exponents, λ_1 and λ_2 , for the non-autonomous form of the HMEH system. The LEDs delimit both periodic (convergent) and chaotic or hyperchaotic regions (divergent). The first is characterized by negative exponents (grayscale region), while chaotic and hyperchaotic regions are characterized by positive exponents (rainbow-colors region). These two LEDs are shown to expose the differentiation between chaotic and hyperchaotic dynamical responses. While chaotic regions show only $\lambda_1 > 0$, hyperchaotic regions present both $\lambda_1 > 0$ and $\lambda_2 > 0$.

Figures 5(b), (d) and (f) show the OPDs for the overall average output power, \bar{P}_{avg} , the average output power of the piezoelectric transducer, \bar{P}_{pz} , and the average output power of the electromagnetic transducer, \bar{P}_{em} . All these quantities are computed considering the steady-state responses ($\tau > \tau_{trans}$) of each time series sample, being essential to define system performance.

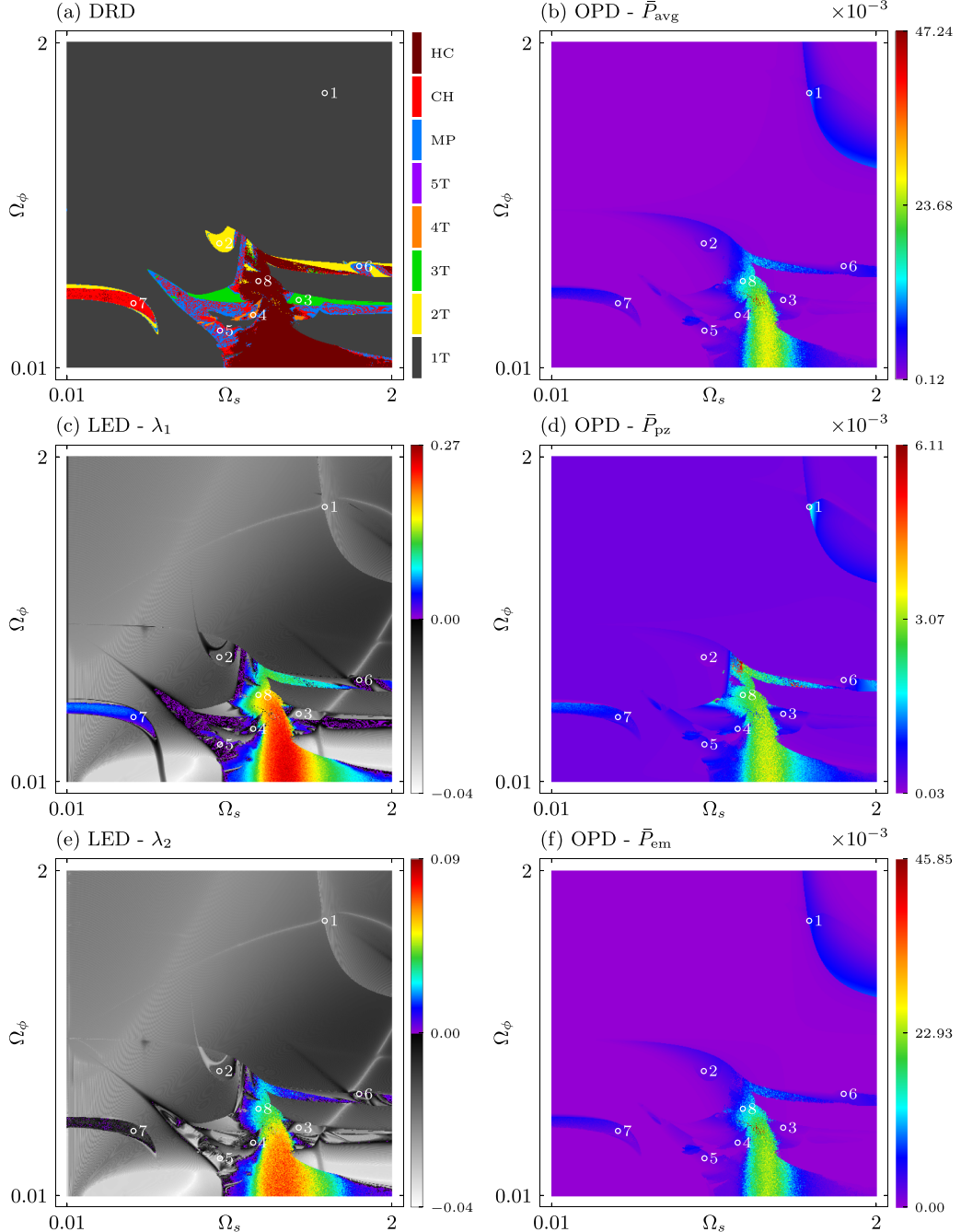


Figure 5. Diagrams for the $\Omega_s \times \Omega_\phi$ parameter space, considering fixed excitation parameters of $\gamma = 0.1$ and $\Omega = 1.2$: (a) DRD showing the classification of distinct types of dynamical responses, color-coded according to text description. (b) OPD for the overall average output power, \bar{P}_{avg} . (c) LED for largest Lyapunov exponent, λ_1 . (d) OPD for the average output power of the piezoelectric transducer, \bar{P}_{pz} . (e) LED for the second largest Lyapunov exponent, λ_2 . (f) OPD for the average output power of the electromagnetic transducer, \bar{P}_{em} . OPD colorbars represent output power values; LEDs colorbars indicate the value of exponents (rainbow colors for positive, grayscale for negative). Each diagram is built with a grid of 500×500 points.

It should be pointed out that the attractors present a predominance of 1T periodic responses, followed by hyperchaotic responses in the bottom right part of the diagrams. The analysis of these diagrams together indicates that more complex regions, associated with many types of dynamical responses, produce better performance, especially the central part of the hyperchaotic zone. Also, this case shows

the output power predominance of the electromagnetic transducer, showing a maximum value of 7.5 times greater than the piezoelectric element.

Eight points, labeled from 1 to 8, are marked on the diagrams to illustrate each dynamical response classified within the DRD. These points are meticulously documented in table 2 for reproducibility. Figure 6 showcases the distinct dynamical

Table 2. Exact corresponding values of Ω_s and Ω_ϕ marked in the diagrams of figure 5 used to exemplify the different dynamical responses in figure 6.

Point	Classification	Ω_s	Ω_ϕ
1	1T	1.589238476953908	1.692925851703407
2	2T	0.943186372745491	0.771703406813627
3	3T	1.429719438877756	0.424749498997996
4	4T	1.150561122244489	0.333026052104208
5	5T	0.947174348697395	0.237314629258517
6	MP	1.80060120240481	0.632124248496994
7	CH	0.416773547094188	0.404809619238477
8	HC	1.18246492985972	0.540400801603206

responses corresponding to each point. Each example is depicted through four steady state phase subspaces: $\dot{x} \times \ddot{x}$, representing the x -direction, $\dot{z} \times \ddot{z}$, representing the z -direction, $\dot{\phi} \times \ddot{\phi}$, representing the pendulum motion. Notably, the ϕ -direction is constrained to the range of the remainder of the actual value of $\dot{\phi}$ divided by 2π . This treatment aligns with the topological view of the pendulum's phase subspace as a cylinder, where π and $-\pi$ represent the same position (upward vertical position) (Savi 2017, Carvalho and Savi 2020). Finally, $\dot{v} \times I$ represents the electrical coordinate domain. It is noticeable that the first seven points, from figures 6(a) to (g), show dynamical behaviors where the pendulum does not rotate, but oscillates between a maximum and a minimum position. A variety of responses are observable with this characteristic, remarkably the quasi-periodic behavior showed in figure 6(f) and the chaotic response in figure 6(g) where the system exhibits a complex aperiodic pattern of motion. Alternatively, the example presented in figure 6(h) shows a hyperchaotic complex response where the pendulum shows an irregular pattern, including rotation. This result indicates that the HMEH exhibits better performance when the pendulum has some kind of high-amplitude motion.

3.3. Global dynamics

In order to determine the best and worst combinations of Ω_s and Ω_ϕ across various excitation scenarios, the analysis presented in figure 5 is conducted across 100 scenarios, each distinguished by different excitation values. Initially, five specific values of γ ranging from $\gamma=0.1$ to $\gamma=0.5$ are selected, with an interval of $\Delta\gamma=0.1$ between each value. Subsequently, for each value of γ , 20 distinct values of parameter Ω are examined, ranging from $\Omega=0.1$ to $\Omega=2$, with an interval of $\Delta\Omega=0.1$. This extensive range allows the evaluation of the system performance under a broader spectrum of excitation conditions. A subset of these scenarios, specifically forty (40), are depicted in figures 7–10.

Figure 7 showcases 20 unique instances of $\Omega_s \times \Omega_\phi$ DRDs, achieved by varying Ω while maintaining a fixed the value of $\gamma=0.1$. It is observed that lower Ω values, represented in the first row of figures 7((a)–(d))—ranging from $\Omega=0.1$ to $\Omega=0.4$ —lead to a simpler system behavior when altering Ω_s and Ω_ϕ , primarily exhibiting 1T dynamical responses. As the excitation frequency increases

from $\Omega=0.5$ to $\Omega=1.2$, the complexity intensifies, especially near the z -direction resonance (around the vicinity of $\Omega=1$). However, a further increase in the excitation frequency from $\Omega=1.3$ to $\Omega=2$ results in a reduction in complexity.

Figure 8 presents the corresponding OPDs for the DRDs depicted in figure 7. Several observations can be made by comparing these two figures. Firstly, an increase in complexity is indicative of improved performance according to these results. Secondly, near z -direction resonance ($0.8 \leq \Omega \leq 1.0$), the regions of good performance expand within the OPDs, as expected. Thirdly, 1T, 2T, and HC responses are the most prevalent dynamical behaviors observed, followed by CH and MP responses. Upon examination of these results, it is noted that the majority of hyperchaotic regions show superior performance, while the majority of 1T regions (though not all) exhibit poor performance. For instance, the top-right regions of figures 8(i)–(l) (from $\Omega=0.9$ to $\Omega=1.2$) show an arc-shaped strip with elevated output power values. In fact, this strip seems to move from the bottom region (figure 8(a)) to the top right region of the diagrams, while other more complex regions emerge at the bottom as Ω increases. Fourthly, the peak power moves from smaller to larger Ω_s values as Ω increases, as expected, due to the change in the beam's resonance frequency region. In this regard, the peak output power region of the OPDs from $\Omega=0.1$ to $\Omega=0.8$ (figures 8(a)–(h)) are well-defined regular 1T attractors. Alternatively, from $\Omega=0.9$ to $\Omega=2$ (figures 8(i)–(t)), the regions that display the best performances are hyperchaotic ones. Finally, as the resonance shifts from a lower to a higher Ω_s value, an increase in maximum average output power, $\bar{P}_{avg}^{(max)}$, is observed in almost all cases.

Several of the previously discussed observations hold for scenarios with a higher excitation amplitude of $\gamma=0.3$, as presented in figures 9 and 10. Nevertheless, some new behaviors also emerge. In this case, due to the larger excitation magnitude, some of the described phenomena start to appear at lower Ω values compared to the previous case. In the scenario with low Ω values from $\Omega=0.1$ to $\Omega=0.3$, the peak power regions are characterized by 1T regular attractors. For $\Omega=0.3$ and $\Omega=0.4$, 2T and CH attractors also appear in the peak output power zone. These attractors form a strip, similar to the one in the previous case, that moves towards the top right region of the diagram.

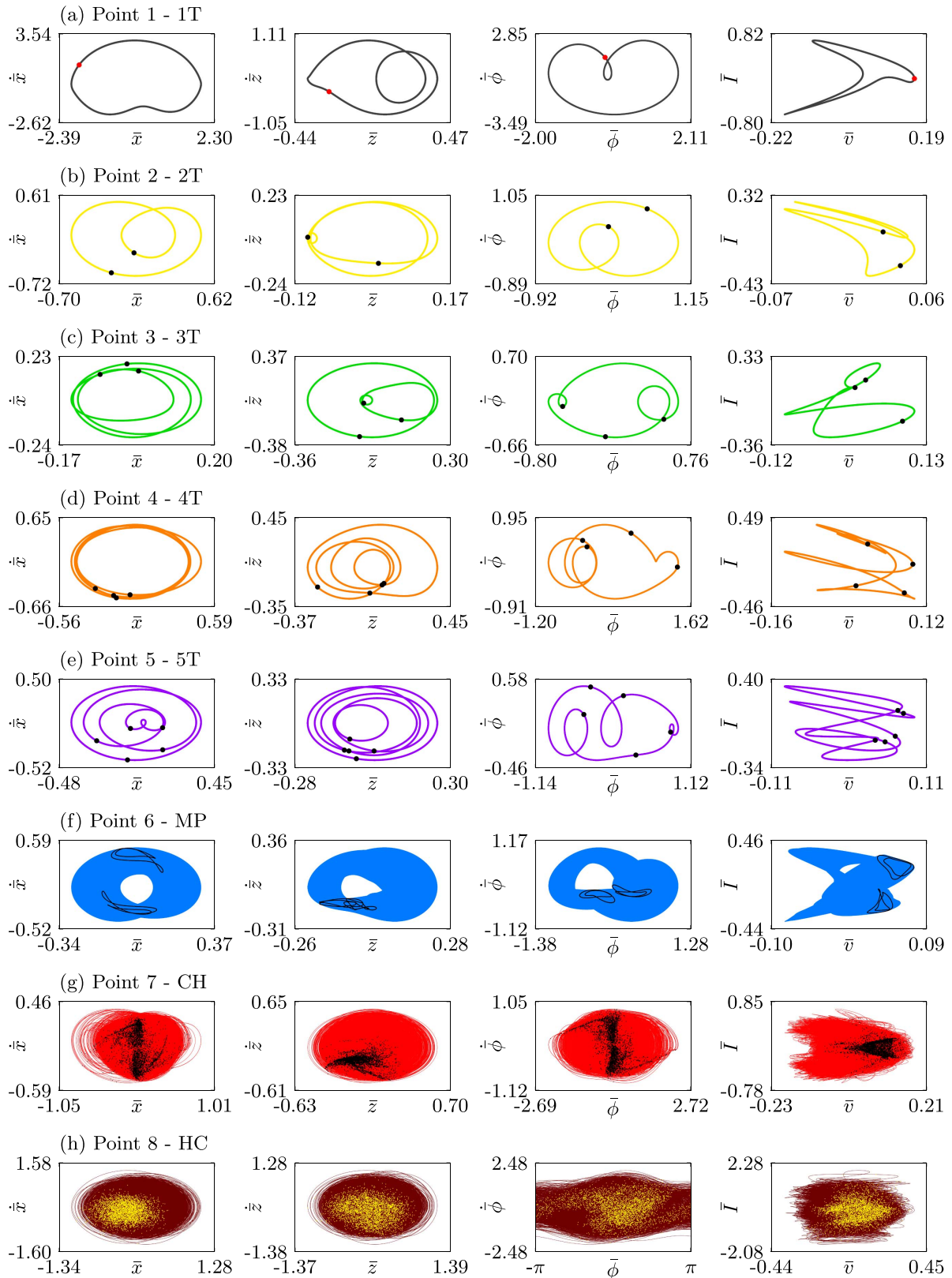


Figure 6. Corresponding phase subspaces and Poincaré maps of the steady-state response of points 1 to 8, as referenced in figure 5 and detailed in table 2. Each color represents distinct dynamical responses. (a) dark gray: 1T, (b) yellow: 2T, (c) light green: 3T, (d) orange: 4T, (e) purple: 5T, (d) light blue: MP - in this case, quasi-periodic, (g) red: chaotic - CH, and (h) dark red: hyperchaotic - HC. Poincaré maps are displayed by black dots, except for red in the 1T case and yellow in the HC case.

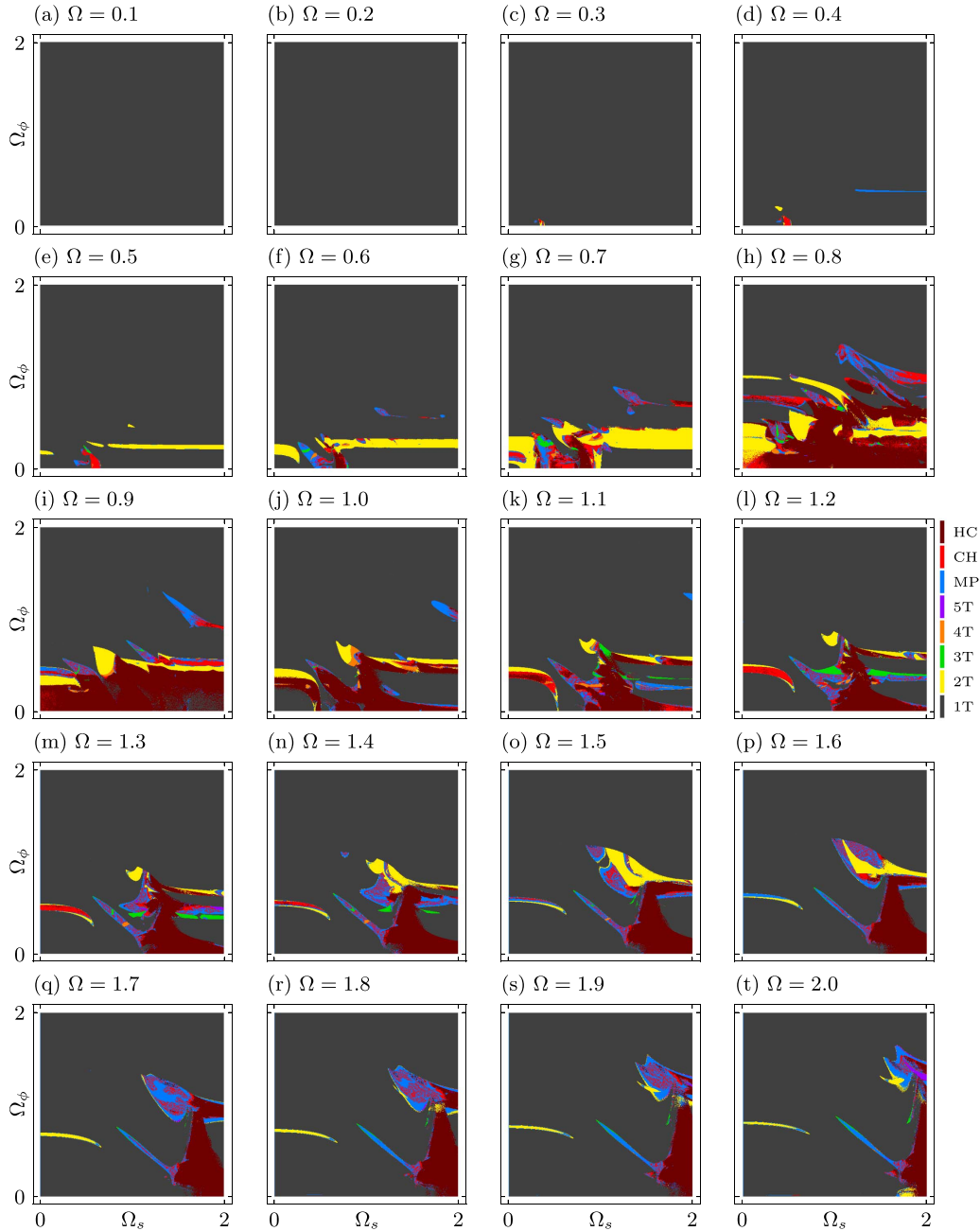


Figure 7. DRDs for a fixed value of excitation amplitude of $\gamma = 0.1$, showing different values excitation frequency, from (a) $\Omega = 0.1$ to (t) $\Omega = 2$, with an interval of $\Delta\Omega = 0.1$. Different colors represent distinct dynamical behaviors summarized in the accompanying colorbar. Each diagram is built with 500×500 sample points.

As Ω increases from $\Omega = 0.4$ to $\Omega = 2$, the complexity increases, and new regions with distinct dynamical responses emerge. From the scenario with $\Omega = 0.4$ to $\Omega = 0.8$ (from figures 10(d) to (h)), high-performance regions (red regions) exhibit a greater number of distinct attractors, but with the 1T attractor being predominant. From $\Omega = 0.9$ to $\Omega = 2$ (from figures 10(i) to (t)), the majority of attractors appearing in high-performance zones (red regions) are aperiodic ones (CH and HC). As before, the increase in Ω shifts the peak output power region to higher Ω_s values due to the change in the system's resonance characteristics. Also, the increase in γ results

in an overall increase in the maximum output power displayed across all scenarios.

3.4. The best key structural parameters

The previous analysis, represented by figures 7–10, provide numerous valuable insights concerning energy harvesting, being useful for design decision making through the determination of the combinations of Ω_s and Ω_ϕ that yields the best performances. Nevertheless, the analysis and design is a complex task that requires more sophisticated tools. An

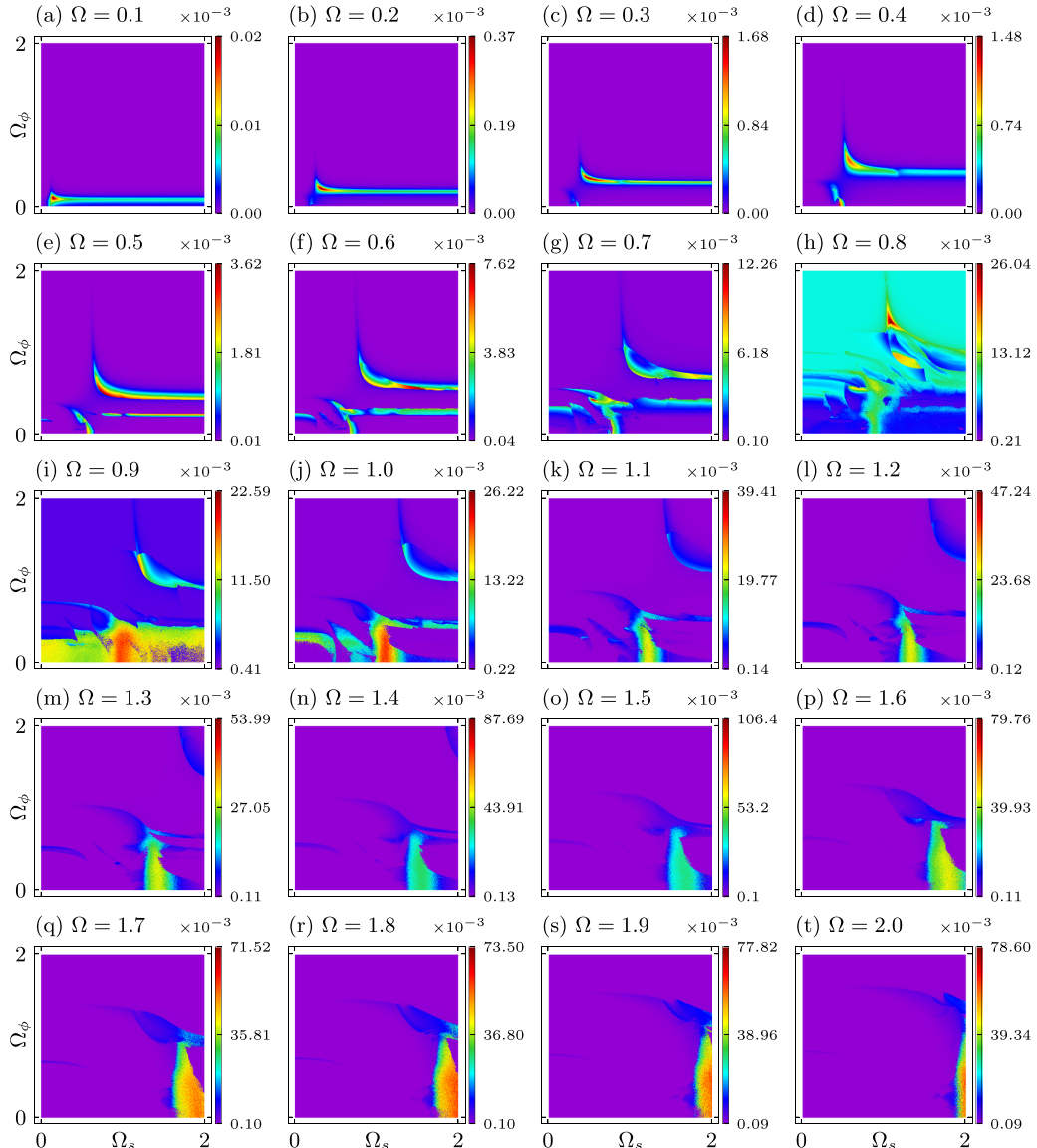


Figure 8. \bar{P}_{avg} OPDs for a fixed value of excitation amplitude of $\gamma = 0.1$, showing different values excitation frequency, from (a) $\Omega = 0.1$ to (t) $\Omega = 2$, with an interval of $\Delta\Omega = 0.1$. Accompanying rainbow colorbars show the range of values of \bar{P}_{avg} for each scenario. Each diagram is built with 500×500 sample points, and linear scale is used in colormap values.

interesting tool is the OCD which is a two-dimensional parameter diagram that monitors how many times a certain characteristic occurs in a certain region of the parameter space (Costa *et al* 2021). A comprehensive explanation of the method used to build the OCDs is provided in appendix A.4. By employing this approach, it is possible to effectively identify regions within the $\Omega_s \times \Omega_\phi$ parameter space where higher and lower performances are more likely to occur.

In the process of analyzing 100 distinct scenarios, each with its unique set of OPDs (one for the \bar{P}_{pz} , one for \bar{P}_{em} and one for \bar{P}_{avg}), it is crucial to normalize the power ranges prior to constructing the OCDs. This normalization ensures that the values representing the lowest and highest performances of each OPD are scaled to 0 and 1, respectively. This step is

necessary as each OPD possesses its own unique minimum and maximum values of average output power, and constructing the OCDs without this normalization could lead to biased results.

The normalization is carried out for three sets of 100 OPDs: one set regarding the average output power of the piezoelectric transducer, \bar{P}_{pz} , one related to the average output power of the electromagnetic transducer, \bar{P}_{em} , and the last concerning the overall average output power of the HMEH, \bar{P}_{avg} . For each point within an OPD, a normalized output power, $\bar{P}_{\text{norm}_{ij}}$, is defined. It is calculated by dividing the average output power, \bar{P}_{ij} , at a specific point within the OPD defined by indices i and j , by the maximum average output power, $\bar{P}^{(\max)}$, which is the highest output power observed within the currently analyzed OPD.

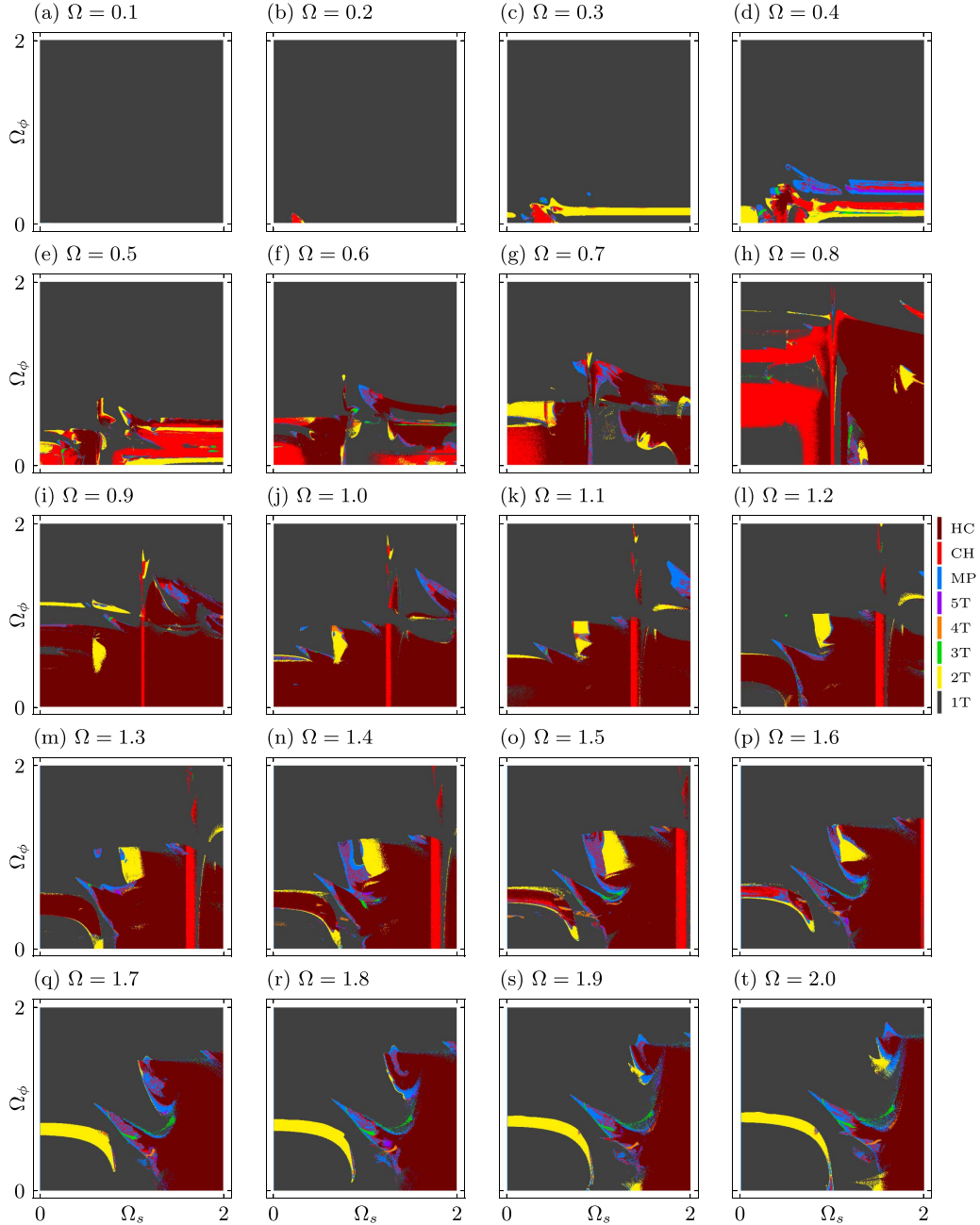


Figure 9. DRDs for a fixed value of excitation amplitude of $\gamma = 0.3$, showing different values excitation frequency, from (a) $\Omega = 0.1$ to (t) $\Omega = 2$, with an interval of $\Delta\Omega = 0.1$. Different colors represent distinct dynamical behaviors summarized in the accompanying colorbar. Each diagram is built with 500×500 sample points.

$$\bar{P}_{\text{norm},ij} = \frac{\bar{P}_{ij}}{\bar{P}(\text{max})}, \quad (i = 1, \dots, 500); (j = 1, \dots, 500) \quad (27)$$

For the current analysis, it has been established that the OCDs should monitor instances where $\bar{P}_{\text{norm}} \geq 0.3$. In other words, any sample within the OPD that exhibits an output power value exceeding 30% of the maximum output power of the current OPD is recorded by the OCD. This threshold is selected as it effectively identifies regions demonstrating good to excellent performance in terms of output power and bandwidth.

The resulting OCDs are displayed in figure 11. Figure 11(c) makes evident that the optimal overall combinations of Ω_s and Ω_ϕ are situated in the bottom right region of the diagrams, while the least favorable combination is located in the top left. Specifically, approximately 60%–68% of the cases with performance exceeding a threshold of 30% ($\bar{P}_{\text{norm}}^{(\text{overall})} \geq 0.3$) occur at higher Ω_s values and lower Ω_ϕ values. Conversely, about 2%–5% of the cases with similar performance levels occur at lower Ω_s values and higher Ω_ϕ values. Moreover, medium occurrence values are displayed at lower to mid-range Ω_ϕ values, spanning all Ω_s values. Additionally, the OCD for the $P_{\text{norm}}^{(em)}$, associated with the electromagnetic

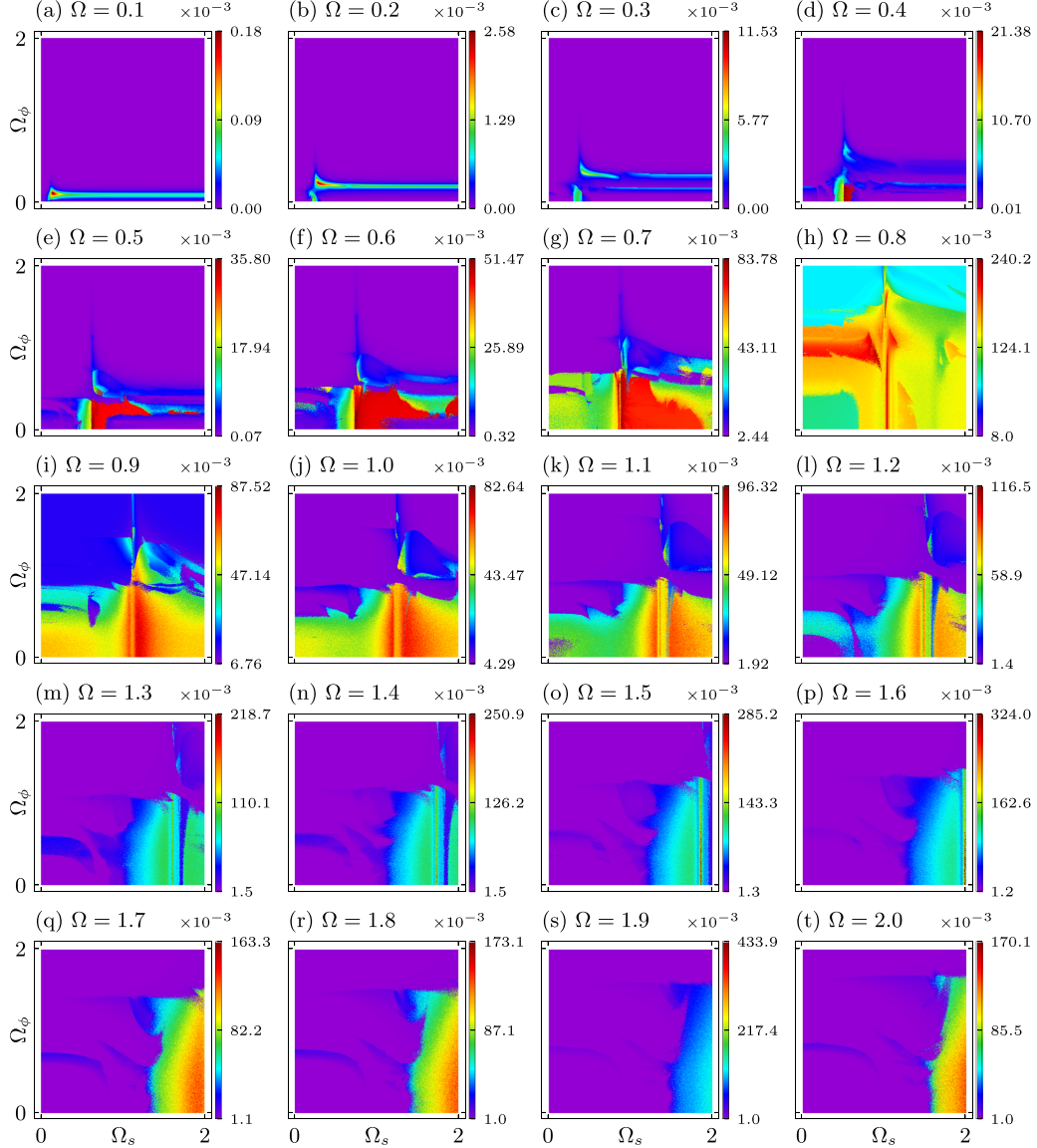


Figure 10. \bar{P}_{avg} OPDs for a fixed value of excitation amplitude of $\gamma = 0.3$, showing different values excitation frequency, from (a) $\Omega = 0.1$ to (t) $\Omega = 2$, with an interval of $\Delta\Omega = 0.1$. Accompanying rainbow colorbars show the range of values of \bar{P}_{avg} for each scenario. Each diagram is built with 500×500 sample points, and linear scale is used in colormap values.

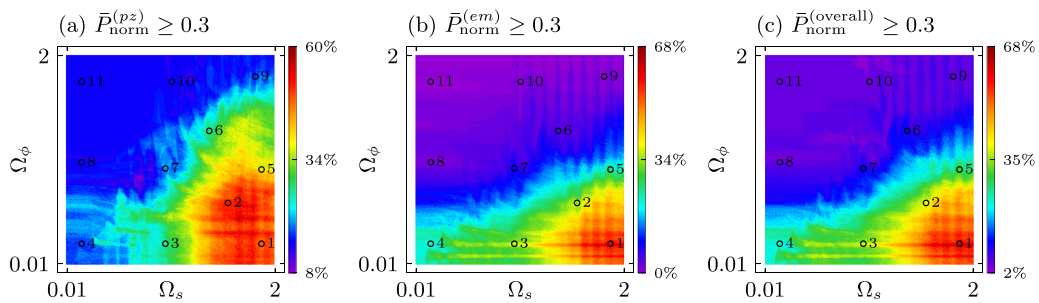


Figure 11. Occurrence Diagrams (OCDs) of the $\Omega_s \times \Omega_\phi$ parameter space for a threshold of (a) $\bar{P}_{\text{norm}}^{(pz)} \geq 0.3$, (b) $\bar{P}_{\text{norm}}^{(em)} \geq 0.3$, and (c) $\bar{P}_{\text{norm}}^{(\text{overall})} \geq 0.3$. The accompanying colorbar in each OCD represents the likelihood of the corresponding threshold to occur. Black circles labeled with numbers from 1 to 11 represent values of combinations of Ω_s and Ω_ϕ of interest. Linear scale is used in colormap values.

Table 3. Exact corresponding values of Ω_s and Ω_ϕ marked in the OCDs of figure 11 used to determine the configurations analyzed in figures 12–14. Region colors are associated with the occurrence percentage as displayed in the OCDs.

Configuration	Ω_s	Ω_ϕ	Region Color in the OCD		
			$\bar{P}_{\text{norm}}^{(pz)}$	$\bar{P}_{\text{norm}}^{(em)}$	$\bar{P}_{\text{norm}}^{(\text{overall})}$
1	1.87	0.20	Orange	Red	Red
2	1.55	0.59	Red	Green	Yellow-green
3	0.95	0.20	Cyan	Yellow	Yellow
4	0.15	0.20	Blue	Cyan	Cyan
5	1.87	0.91	Yellow	Cyan	Green
6	1.37	1.28	Green	Blue	Blue
7	0.95	0.92	Blue	Blue	Blue
8	0.15	0.98	Blue	Purple	Purple
9	1.81	1.80	Blue	Purple	Purple
10	1.01	1.75	Blue	Purple	Purple
11	0.15	1.75	Blue	Purple	Purple

transducer, exhibits similar qualitative behavior, as depicted in figure 11(b). Alternatively, figure 11(a) presents the OCD for the $\bar{P}_{\text{norm}}^{(pz)}$, associated with the piezoelectric transducer. Although the region of high occurrence of good performance still appears in the bottom right region of the OCD, it covers a larger area within the diagram. Also, the regions of medium occurrence values are dispersed around the high occurrence region, occupying a range of approximately $0.7 \leq \Omega_s \leq 1.3$ and $0.01 \leq \Omega_\phi \leq 1.8$.

In summary, this discussion reveals that an MHEH with a stiffer x direction, k_x , and a longer pendulum length, L_p , outperforms an HMEH with opposite configurations. To corroborate this point, 11 configurations are selected within the OCDs, each possessing unique structural characteristics (distinct Ω_s and Ω_ϕ values). The location of these configurations within the OCD is marked as black circles labeled from 1 to 11, as displayed in figure 11, and listed in table 3 for reproducibility. For each configuration, a new set of DRDs and OPDs are constructed within the $\gamma \times \Omega$ parameter space to assess performance under a broad range of external excitation conditions, where the values of γ are varied from 0.01 to 0.5, and the values of Ω are varied from 0.01 to 2, both contained in a grid of 1000×1000 points. In this regard, many aspects of this analysis are visual representations of a qualitative characteristic, with different colors or gradients representing different characteristics. Consequently, in this analysis, any output power value classified from blue to red is considered part of the harvester's operational bandwidth, while purple values are considered poor performance.

Figure 12 showcases the result for Configurations 1, 2, 3, and 5. These configurations reside in the region of medium to high occurrences of $\bar{P}_{\text{norm}} \geq 0.3$ in the OCDs, spanning from green to red-colored regions. Each case displays the DRD, the OPD, and the percentage contribution of each transducer to the average output power of the OPD. Here, EM (light red bar) represents the electromagnetic transducer, and PZ (orange bar) represents the piezoelectric transducer. Overall, this first set of configurations exhibits a wider bandwidth characterized by complex dynamical patterns, observable even at

the lowest excitation amplitude values. Upon visual examination and comparison of the DRDs with the OPDs of each case, regions of good performance are characterized by complex dynamical patterns, especially hyperchaotic (HC) attractors. The majority of poor performance regions are associated with 1T regular responses. 2T and chaotic (CH) are also common and appear in certain clusters within the parameter domain. The main peak power occurs in a concentrated region (labeled as A) associated with the resonance of the \bar{z} -direction, followed by a secondary peak (labeled as B) associated with the resonance of the \bar{x} -direction that transmits more energy to the pendulum. This secondary peak arises in different positions of the diagram and is associated with the value of Ω_s . That is, a configuration with higher Ω_s presents a secondary peak at higher excitation amplitudes, and vice-versa. Configuration 1 presents the wider bandwidth, while configuration 3 presents the highest maximum output power, despite the reduced bandwidth. Additionally, for all cases in this set of configurations, the electromagnetic transducer predominantly contributes to the power conversion of the HMEH.

Figure 13 presents results of Configurations 4, 6 and 7. These configurations are situated in the blue regions (both light and navy blue) of the $\bar{P}_{\text{norm}}^{(\text{overall})}$ and $\bar{P}_{\text{norm}}^{(em)}$ OCDs of figures 11(b) and (c), and in the blue to green regions of the $\bar{P}_{\text{norm}}^{(pz)}$ OCD of figure 11(a). In this set of configurations, it is observed that the complex regions associated with higher performances are distributed in small clusters, showing a reduced, yet significant, bandwidth. Moreover, the maximum output powers achieved surpass those of the majority of the previous configurations presented in figure 12. They are concentrated in the \bar{z} -direction resonance region. Additionally, these configurations exhibit a more balanced distribution of converted power between the two transducers.

On the other hand, figure 14 presents a set of four configurations that are located in the blue regions of the $\bar{P}_{\text{norm}}^{(pz)}$ OCD in figure 11(a), and in the purple regions of the remaining OCDs in figures 11(b) and (c). In general, these configurations are characterized by the dominance of the piezoelectric

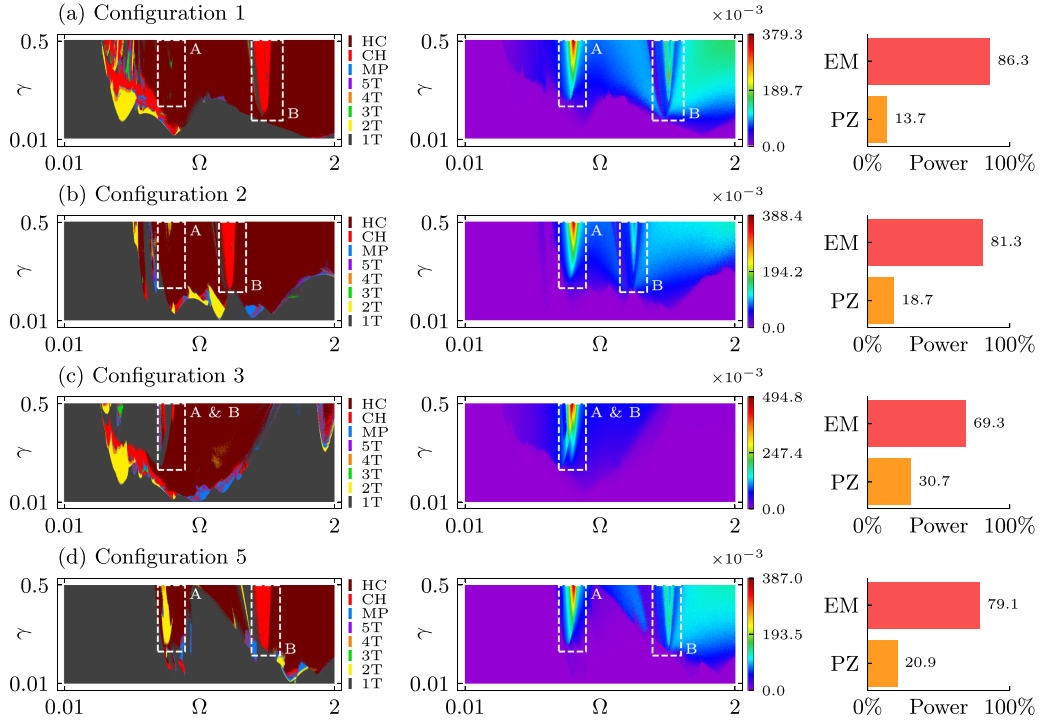


Figure 12. DRD, OPD for the overall average output power, \bar{P}_{avg} , and the contribution of each transducer in the power conversion for (a) Configuration 1, (b) Configuration 2, (c) Configurations 3, and (d) Configuration 5. DRD colorbars represent different types of dynamical responses, and OPD colorbars represent a range of average output powers displayed by each configuration. Light red and orange bars represent the percentage contribution of the piezoelectric and electromagnetic transducers in the overall conversion, respectively. Each diagram is constructed with a grid of 1000×1000 points of the $\gamma \times \Omega$ parameter space. Linear scale is used in OPDs colormap values.

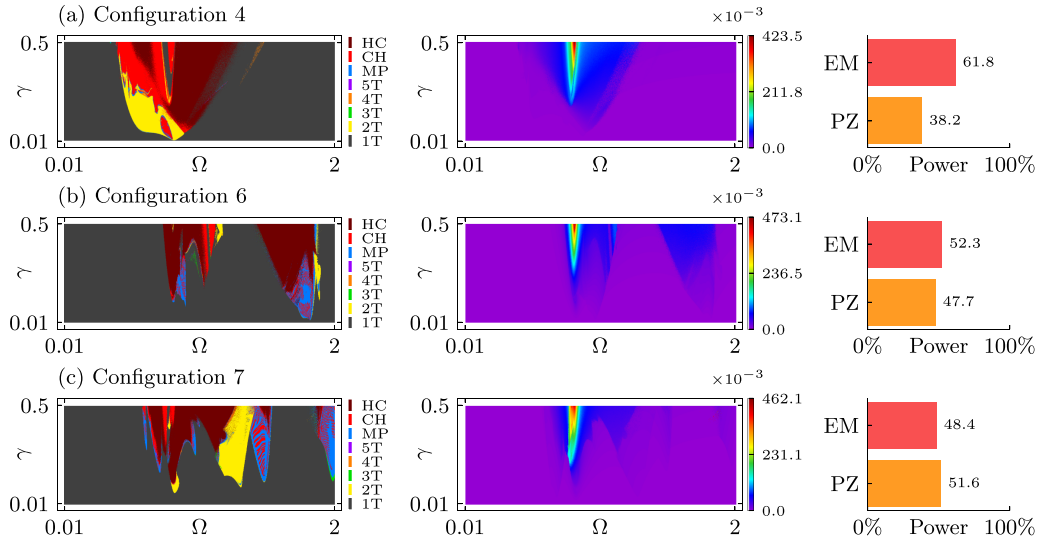


Figure 13. DRD, OPD for the overall average output power, \bar{P}_{avg} , and the contribution of each transducer in the power conversion for (a) Configuration 4, (b) Configuration 6, and (c) Configurations 7. DRD colorbars represent different types of dynamical responses, and OPD colorbars represent a range of average output powers displayed by each configuration. Light red and orange bars represent the percentage contribution of the piezoelectric and electromagnetic transducers in the overall conversion, respectively. Each diagram is constructed with a grid of 1000×1000 points of the $\gamma \times \Omega$ parameter space. Linear scale is used in OPDs colormap values.

transducer in energy conversion. In fact, Configurations 10 and 11 exhibit a predominance exceeding 96%. They also display very narrow bandwidths associated with the peak power in the \bar{z} -direction resonance region, except for Configuration 9,

which shows another narrow secondary peak at higher excitation frequencies due to the higher Ω_s values. This group of configurations represents the worst-case scenario in the utilization of HMEH, as it offers minimal advantages in terms

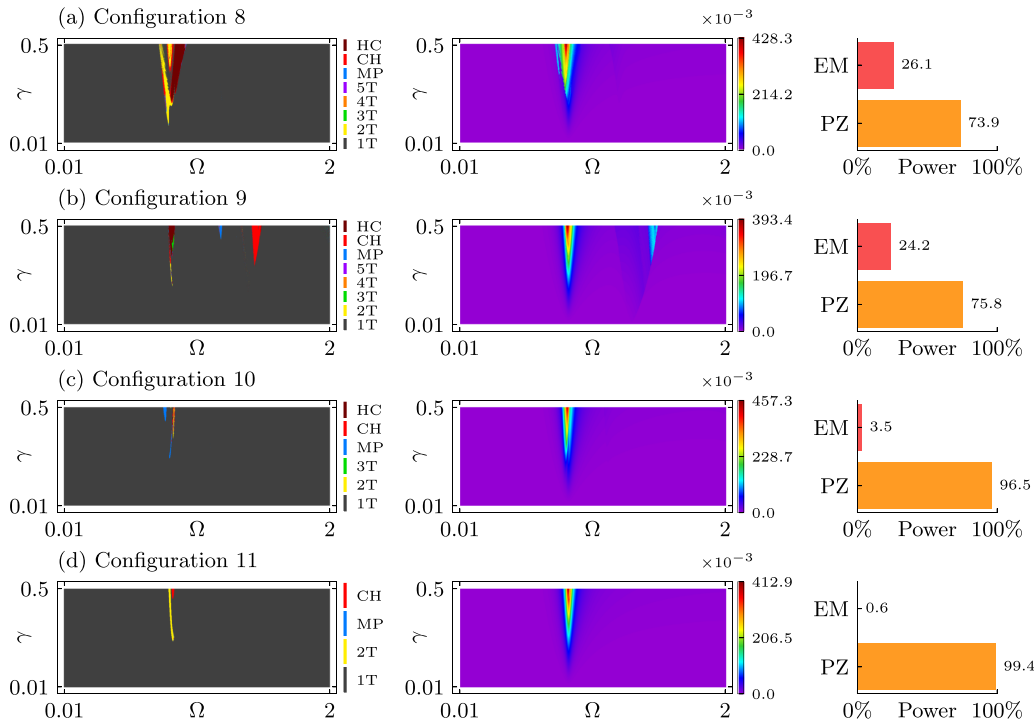


Figure 14. DRD, OPD for the overall average output power, \bar{P}_{avg} , and the contribution of each transducer in the power conversion for (a) Configuration 8, (b) Configuration 9, (c) Configurations 10, and (d) Configuration 11. DRD colorbars represent different types of dynamical responses, and OPD colorbars represent a range of average output powers displayed by each configuration. Light red and orange bars represent the percentage contribution of the piezoelectric and electromagnetic transducers in the overall conversion, respectively. Each diagram is constructed with a grid of 1000×1000 points of the $\gamma \times \Omega$ parameter space. Linear scale is used in OPDs colormap values.

of performance when attaching the pendulum to the classic piezoelectric energy harvester (CPEH).

The analysis outlined in this subsection demonstrates that the OCD is a powerful tool for mapping and determining the optimal and suboptimal combinations of parameters within a specific parameter space. Despite its substantial computational resource requirements, needing the prior assembly of a considerable number of diagrams for its accurate construction, the OCD offers an effective method to map and identify the frequency of occurrence of key characteristics of a dynamical system.

3.5. Dynamical patterns vs performance

The correlation between dynamics and performance is an essential key to the energy harvesting analysis. In this regard, it is important to identify the types of responses and patterns. Besides, it is interesting to evaluate the influence of pendulum incorporation on the harvester response that indeed has demonstrated the potential to significantly enhance operational bandwidth, as presented in figures 12–14. On this basis, one of the key points to address is to identify which pendulum dynamical patterns produce these regions of enhanced performance. To this end, figure 15 presents the concept of a DPD for Configuration 1. A DPD is an extension of the DRD that accounts for the classification and mapping of specific dynamical patterns of a dynamical system in a two-dimensional parameter space. In this case, the DPDs monitor

whether the pendulum rotates or not. Six patterns are identified (see appendix for the criteria):

- RO (Light Cyan): the pendulum oscillates with regular motion and does not rotate;
- IO (Dark Cyan): the pendulum oscillates with an irregular motion, and does not rotate;
- RR (Light Lime Green): the pendulum rotates with a regular motion;
- IR (Lime Green): the pendulum rotates with an irregular motion;
- RM (Light Salmon): the pendulum presents a regular intermittent mix of oscillatory and rotatory motions.
- IM (Lava Red): the pendulum presents a mix of oscillatory and rotatory irregular motions.

Each pattern is exemplified by selected points, labeled with numbers from 1 to 6, as marked by black circles within the DPD in figure 15(a). Four phase subspaces and Poincaré maps ($\bar{x} \times \dot{\bar{x}}$, $\bar{z} \times \dot{\bar{z}}$, $\bar{\phi} \times \dot{\bar{\phi}}$, and $\bar{v} \times \bar{I}$) for each point are depicted in figures 15(b)–(g), representing each different pattern. The color of each phase subspace is associated with the color used to classify the pattern, and the exact γ and Ω values used for the selected points are described in table 4 for reproducibility. Further details about the construction of the DPDs are provided in appendix A.3.

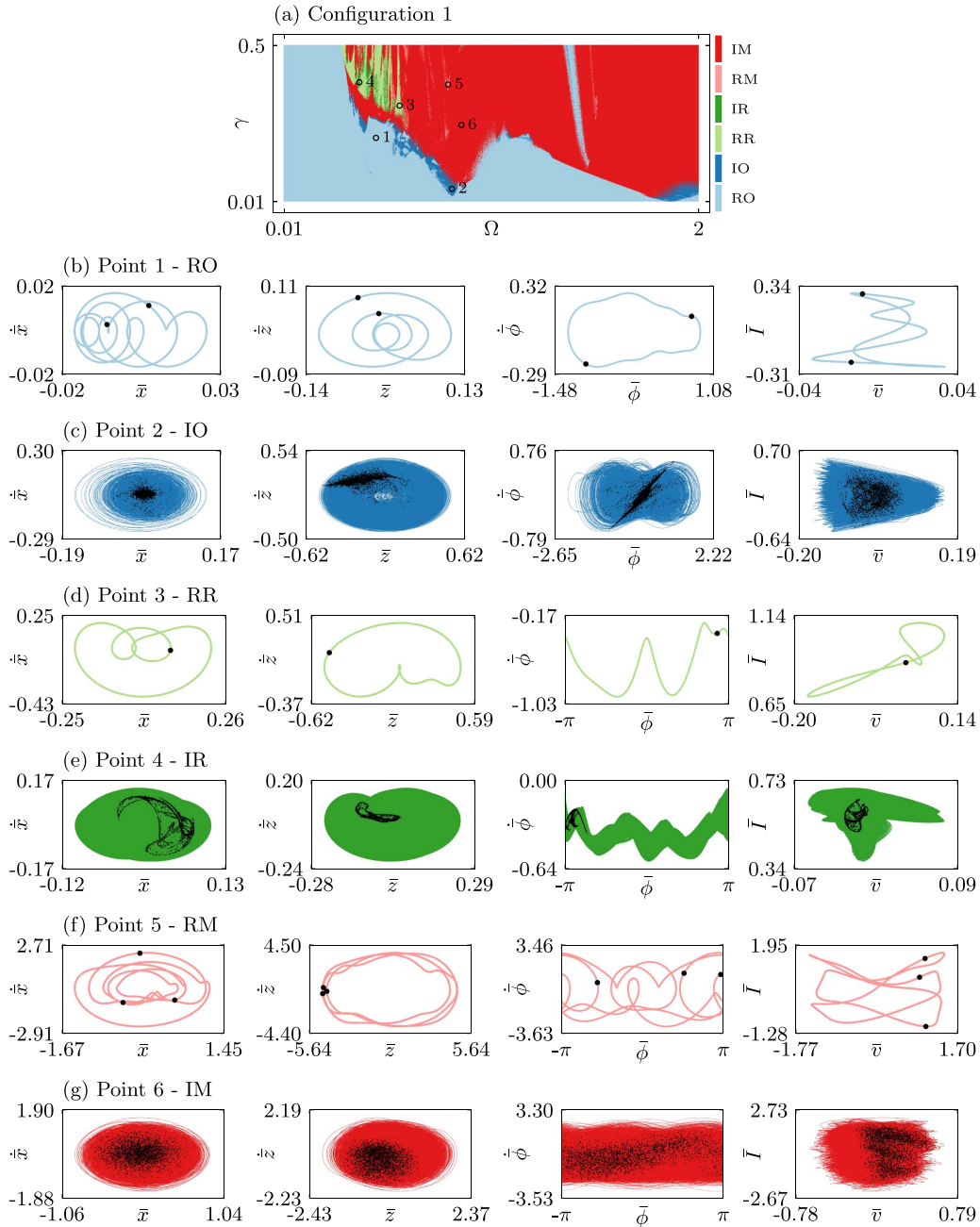


Figure 15. Classification of different pendulum dynamical patterns. (a) Dynamical Pattern Diagrams (DPD) of Configuration 1 for the classification of six different types of patterns: RO (light cyan color) stands for ‘Regular Oscillation’, IO (dark cyan color) stands for ‘Irregular Oscillation’, RR (light lime green) stands for ‘Regular Rotation’, IR (lime green color) stands for ‘Irregular Rotation’, RM (light salmon color) stands for ‘Regular Mixed’, and IM (lava red color) stands for ‘Irregular Mixed’. Points marked as black circles are associated with different patterns. Phase subspaces representation of the (b) RO pattern (point 1), (c) IO pattern (point 2), (d) RR pattern (point 3), (e) IR pattern (point 4), (f) RM pattern (point 5), and (g) IM pattern (point 6). The DPD is constructed with a grid of 1000×1000 points of the $\gamma \times \Omega$ parameter space.

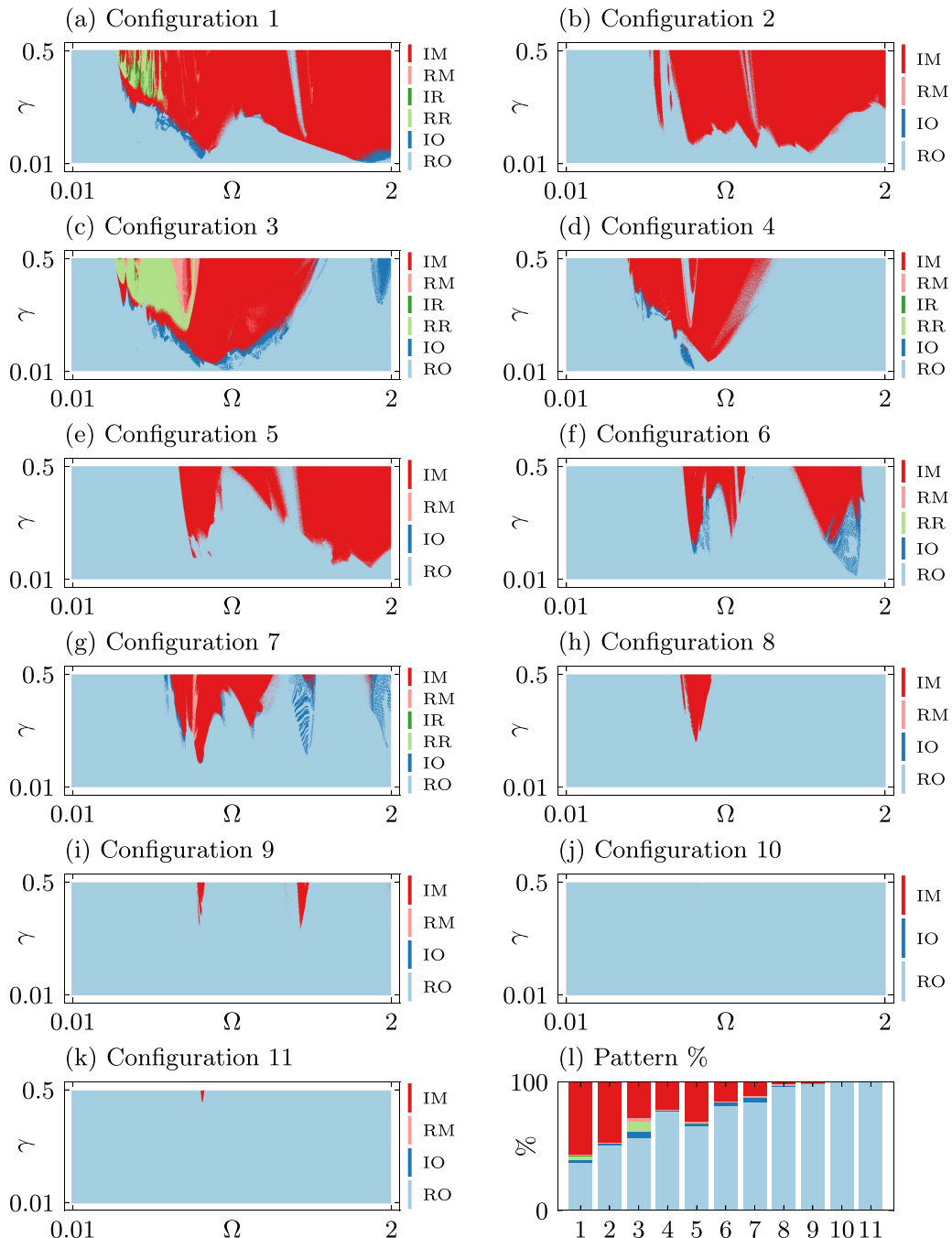
Figure 16 presents a series of DPDs associated with each configuration previously described in table 2. By comparing with the OPDs previously presented in figures 12–14, it is noticeable that triggering a rotational or a mixed dynamical pattern in the pendulum results in an enhanced performance outside the typical \bar{z} -direction resonance zone due to the contribution of the electromagnetic transducer. In fact, this is the reason for the configurations with larger bandwidths

display a greater contribution to energy conversion from the electromagnetic transducer. Furthermore, figure 16(l) supports the previous conclusions by showing the percentage of each dynamical pattern within the DPD for each distinct configuration.

Another crucial topic is the type of dynamical response that yields the best performances. In this regard, from the 100 unique scenarios examined in section 3.3, the total percentage

Table 4. Exact corresponding values of γ and Ω marked in the DPD of figure 15 used to exemplify the different dynamical patterns.

Point	Classification	γ	Ω
1	RO	0.21012012012012	0.45023023023023
2	IO	0.05022022022022	0.814764764764765
3	RR	0.311161161161161	0.563773773773774
4	IR	0.384244244244244	0.370550550550551
5	RM	0.377377377377377	0.796836836836837
6	IM	0.25034034034034	0.860580580580581

**Figure 16.** Dynamical Patterns Diagrams (DPDs) for the classification of six different types of pendulum dynamical patterns. The DPDs are associated with (a) Configuration 1, (b) Configuration 2, (c) Configuration 3, (d) Configuration 4, (e) Configuration 5, (f) Configuration 6, (g) Configuration 7, (h) Configuration 8, (i) Configuration 9, (j) Configuration 10, (k) Configuration 11. Each diagram is constructed with a grid of 1000×1000 points of the $\gamma \times \Omega$ parameter space. (l) Percentage of occurrence of each type of pattern for each configuration.

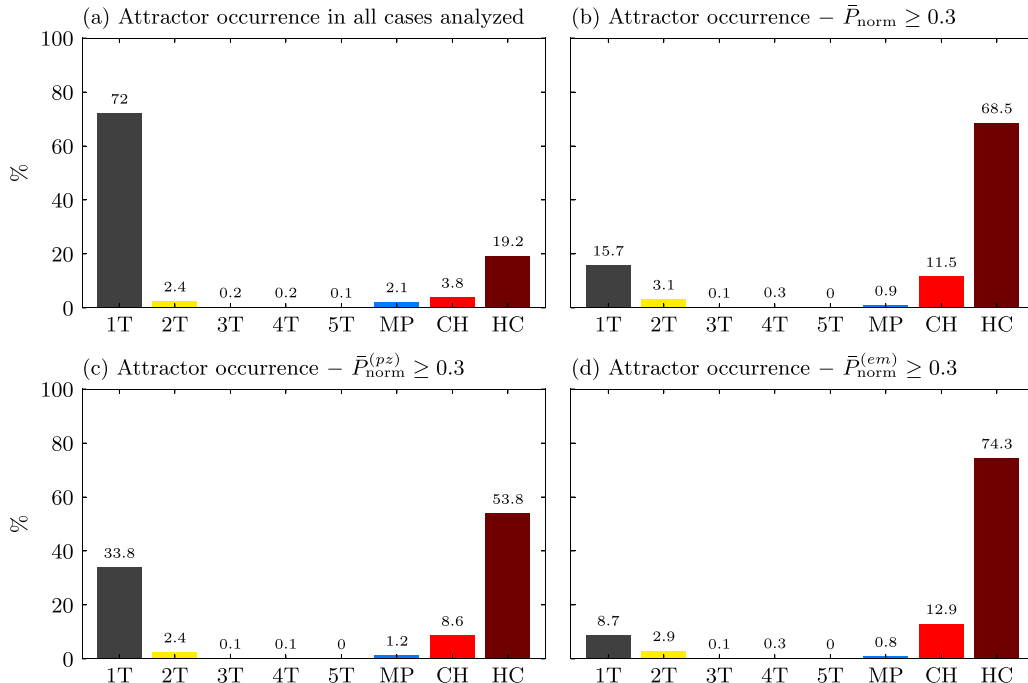


Figure 17. Percentage of dynamical responses for the 100 scenarios studied in section 3.3. (a) Overall percentage with no filter, (b) Percentage of attractors using the filter threshold of $\bar{P}_{\text{norm}} \geq 0.3$ considering the two transducers. (c) Percentage of attractors using the filter threshold of $\bar{P}_{\text{norm}}^{(pz)} \geq 0.3$ considering only the piezoelectric transducer. (d) Percentage of attractors using the filter threshold of $\bar{P}_{\text{norm}}^{(em)} \geq 0.3$ considering only the electromagnetic transducer. Each color represents a distinct dynamical response. Overall, 25×10^6 time series considering unique combinations of 4 key parameters were used in the analysis.

of attractors is accounted for, as displayed in figure 17(a). In essence, 25×10^6 time series, considering different combination of γ , Ω , Ω_s and Ω_ϕ parameters, are analyzed. It is observed that 72% of the dynamical responses are regular 1T attractors, followed by 19.2% of hyperchaotic (HC) ones. Chaotic (CH), 2T and MP also appear in smaller quantities. Additionally, the amount of 3T, 4T and 5T attractors is very small compared to the others. When the same analysis is performed, but only accounting for the dynamical responses that are above the threshold of $\bar{P}_{\text{norm}} \geq 0.3$, as done in the OCD analysis, the scenario reverses, as presented in figure 17(b). In this case, the predominant attractor becomes the hyperchaotic (HC) with 68.5%, followed by 15.7% of 1T attractors, and by 11.5% of Chaotic (CH) responses. The remaining dynamical responses stay relatively the same. Additionally, the same analysis with the same threshold is performed for each transducer, as indicated in figures 17(c) and (d). It is observed that the number of hyperchaotic responses increases and the 1T responses decrease even more for the electromagnetic transducer. Conversely, 1T attractors increase and hyperchaotic attractors decrease for the piezoelectric transducer.

To further investigate the regions of high performance and corroborate the findings presented in figure 17, two configurations from each of figures 12–14 are selected. For each chosen configuration, the overall average maximum output power, $\bar{P}_{\text{avg}}^{(\text{max})}$, for each value of excitation amplitude, γ , is marked as colorful points in the corresponding configuration OPD, as showed in figures 18–20. Grayscale colors within the

OPDs are used to reference the overall lower and higher output powers. Colored points are the points of maximum output power for each distinct value of γ , with the accompanying colorbar indicating their magnitude. The colorbars are truncated within 50% of their maximum value for better representation. The maximum output power magnitudes for each configuration are displayed at the top of the pointing end of the colorbars. Constant values of γ ($\gamma \approx 0.1$, $\gamma \approx 0.2$ and $\gamma \approx 0.3$) are selected, labeled with capital letters, and plotted below the OPDs to display the bandwidths at each selected magnitude of excitation. For each of the three selected values of γ , its respective point of maximum is marked as red circles and labeled with a number from 1 to 3. Their respective phase subspaces and Poincaré maps are built: $\bar{x} \times \dot{\bar{x}}$, representing the x -direction, $\bar{z} \times \dot{\bar{z}}$, representing the z -direction, $\bar{\phi} \times \dot{\bar{\phi}}$, representing the angular subspace of the pendulum, and $\bar{v} \times \dot{\bar{I}}$ representing the electrical coordinate domain.

Specifically, figure 18 depicts Configurations 1 and 2, where the electromagnetic transducer predominantly contributes to energy conversion. The OPDs for these two cases are represented in figures 18(a) and (b), demonstrating that the points of maximum are clustered near the resonance regions. Figures 18(b) and (c) present the frequency response for each selected fixed γ , more clearly illustrating the wider bandwidth associated with these configurations for distinct discrete magnitudes of excitation. From figure 18(e) to (j), one can observe the associated phase subspaces and Poincaré maps of each point of maximum marked in figures 18(b) and (c). These subspaces support the findings associated with figures 16 and 17,

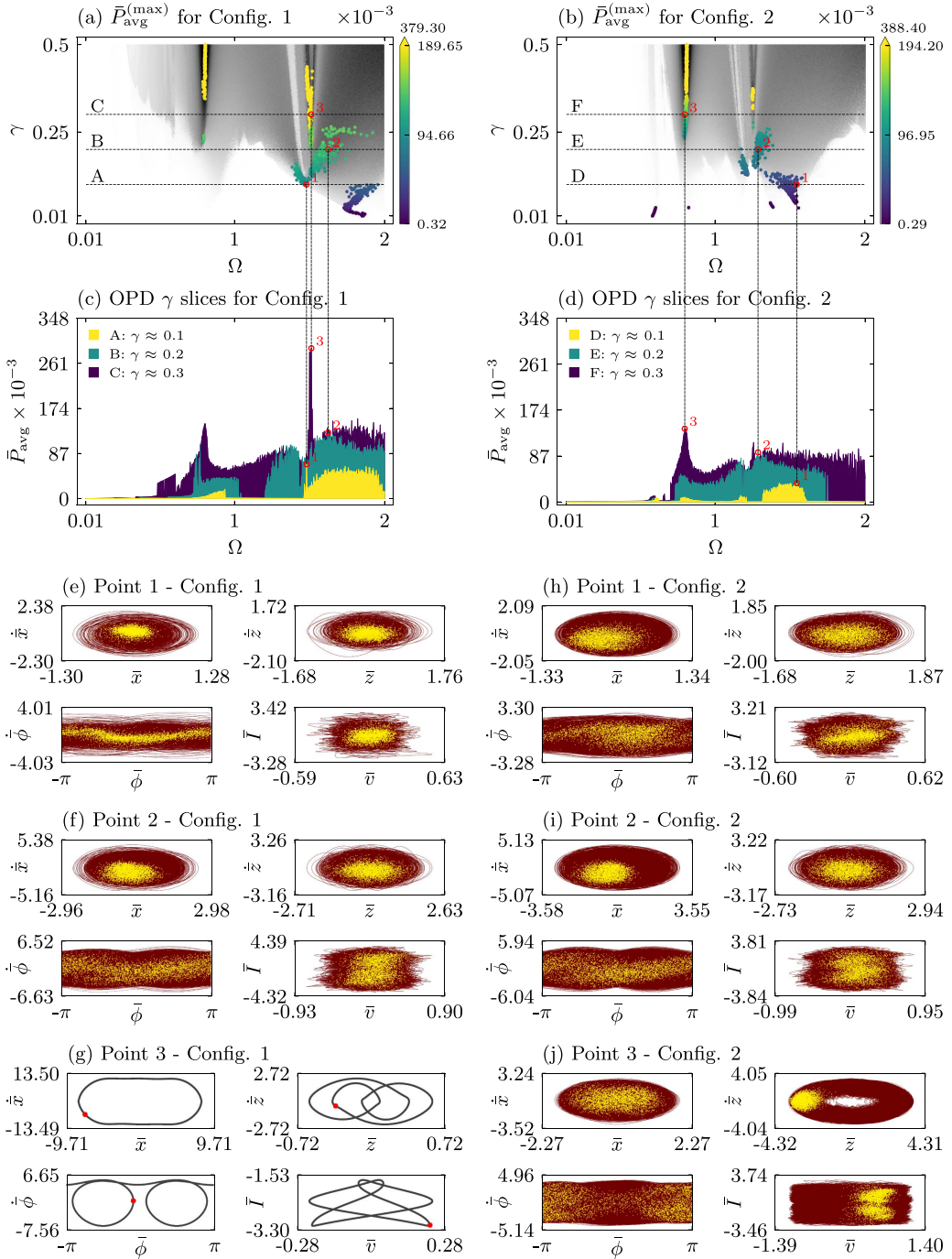


Figure 18. Maximum overall average output power, $\bar{P}_{\text{avg}}^{(\text{max})}$, as a function of γ for (a) Configuration 1 and (b) Configuration 2. Panels (c) and (d) display the slices A, B, C, and D, E, F, respectively of the OPDs for 3 values: $\gamma \approx 0.1$, $\gamma \approx 0.2$ and $\gamma \approx 0.3$. Red circles denote the $\bar{P}_{\text{avg}}^{(\text{max})}$ of each slice. Four phase subspaces ($\dot{x} \times \ddot{x}$, $\dot{z} \times \ddot{z}$, $\dot{\phi} \times \ddot{\phi}$, and $\dot{v} \times \ddot{I}$) and their Poincaré maps of the steady-state response are shown representing red points (e) 1, (f) 2, and (g) 3 for Configuration 1, and red points (h) 1, (i) 2, and (j) 3 for Configuration 2. Phase subspaces' colors represent the color code used in the entire work. The non-maximum values in the OPDs are plotted in grayscale in (a) and (b).

indicating that the dynamical responses associated with the best performances are the hyperchaotic (HC) and 1T attractors, respectively. Also, these performances must be associated with the triggering of the pendulum's rotation or mixed dynamical pattern, as all the selected points of maximum show this characteristic, as highlighted in the $\dot{\phi} \times \ddot{\phi}$ phase subspaces.

Figure 19 presents the same analysis for Configurations 4 and 6, where the contribution of both transducers is balanced. In this scenario, the points of maximum within the OPDs are more concentrated in a single cluster, resulting in narrower, yet still significant, bandwidths. This is further illustrated by the frequency response for each selected value of γ , as presented in figures 19(c) and (d). The phase

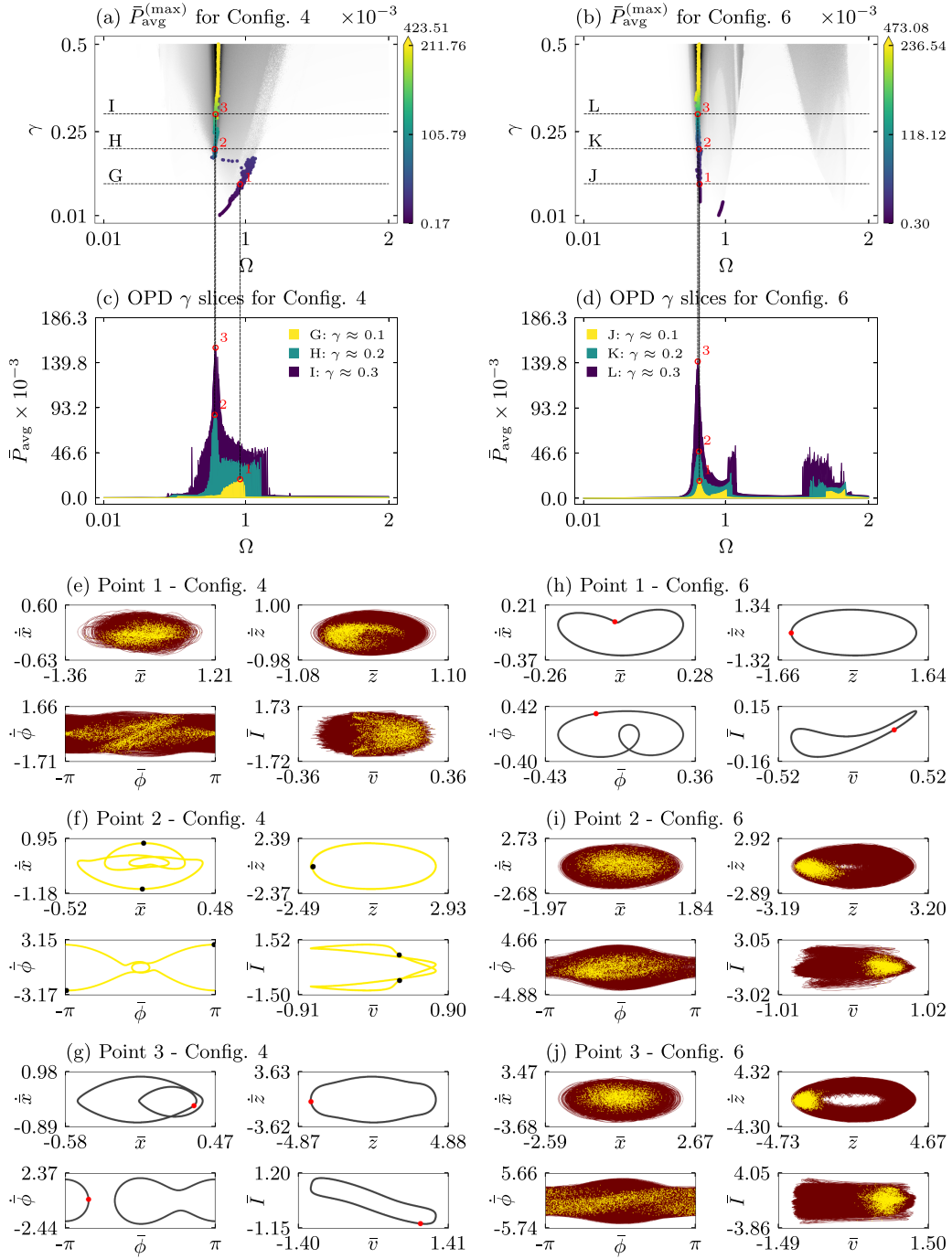


Figure 19. Maximum overall average output power, $\bar{P}_{\text{avg}}^{(\text{max})}$, as a function of γ for (a) Configuration 4 and (b) Configuration 6. Panels (c) and (d) display the slices G, H, I, and J, K, L, respectively of the OPDs for 3 values: $\gamma \approx 0.1$, $\gamma \approx 0.2$ and $\gamma \approx 0.3$. Red circles denote the $\bar{P}_{\text{avg}}^{(\text{max})}$ of each slice. Four phase subspaces ($\dot{x} \times \ddot{x}$, $\dot{z} \times \ddot{z}$, $\dot{\phi} \times \ddot{\phi}$, and $\dot{v} \times \ddot{I}$) and their Poincaré maps of the steady-state response are shown representing red points (e) 1, (f) 2, and (g) 3 for Configuration 4, and red points (h) 1, (i) 2, and (j) 3 for Configuration 6. Phase subspaces, colors represent the color code used in the entire work. The non-maximum values in the OPDs are plotted in grayscale in (a) and (b).

subspaces associated with the selected red points of maximum exhibit a consistent behavior, with more hyperchaotic responses than periodic ones, as displayed from figures 19(e) and (f). Figure 19(f) is particularly noteworthy as it shows a 2T regular response at a point of maximum, representing 3.1% of the high-performance responses above the $\bar{P}_{\text{norm}} \geq 0.3$ threshold. Furthermore, another fact to highlight is that two of the six selected red points of maximum do not show

pendulum rotation. The first is depicted in figure 19(g), showing a high-amplitude regular oscillatory dynamical pattern (RO), and the second is displayed in figure 19(h), showing also RO pattern, but with low amplitude. The latter point corresponds to the point of maximum of the J slice (yellow curve) showing that the high-amplitude pendulum's motion, in this case, commences at higher excitation levels.

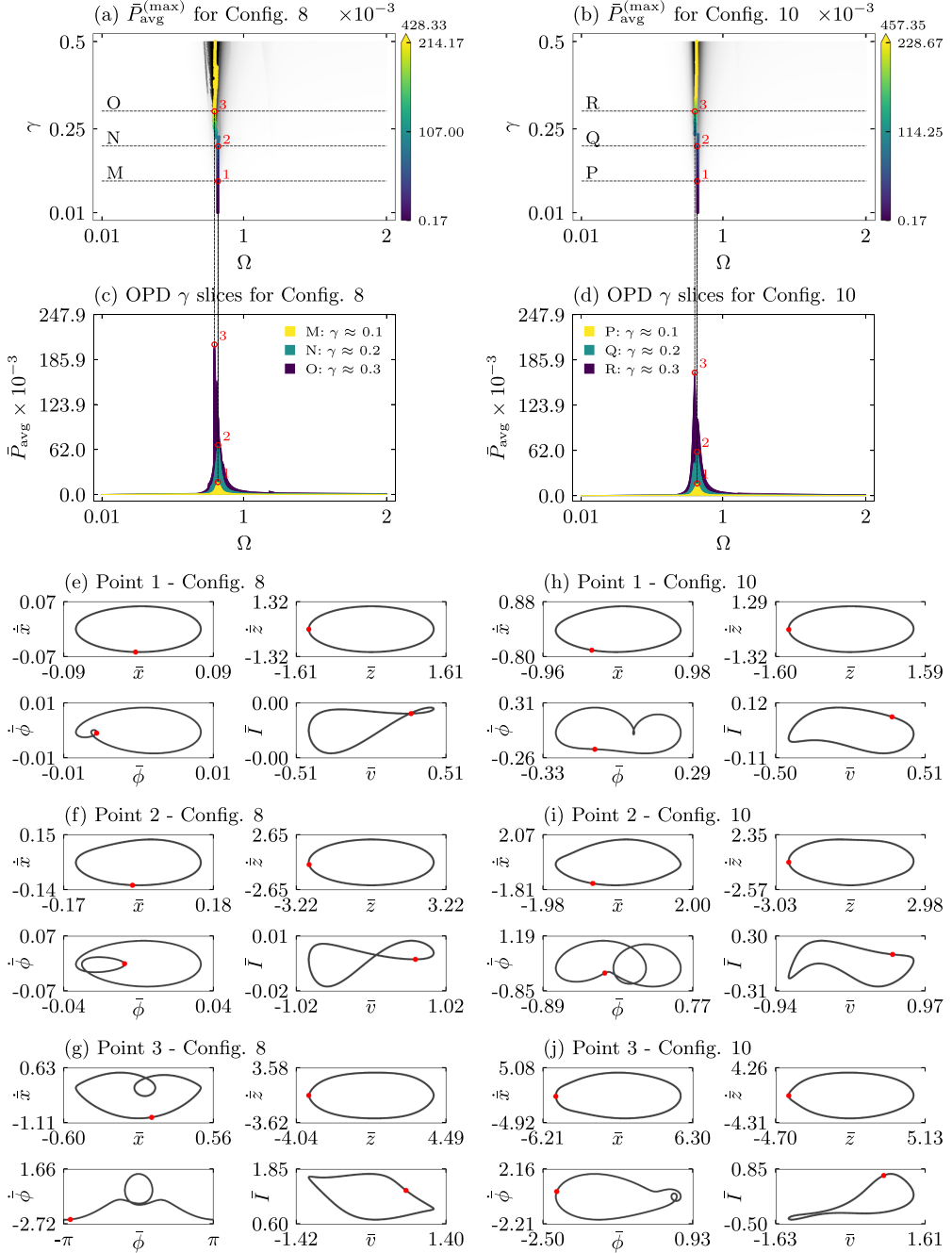


Figure 20. Maximum overall average output power, $\bar{P}_{\text{avg}}^{(\text{max})}$, as a function of γ for (a) Configuration 8 and (b) Configuration 10. Panels (c) and (d) display the slices M, N, O, and P, Q, R, respectively of the OPDs for 3 values: $\gamma \approx 0.1$, $\gamma \approx 0.2$ and $\gamma \approx 0.3$. Red circles denote the $\bar{P}_{\text{avg}}^{(\text{max})}$ of each slice. Four phase subspaces ($\bar{x} \times \dot{\bar{x}}, \bar{z} \times \dot{\bar{z}}, \bar{\phi} \times \dot{\bar{\phi}}$, and $\bar{v} \times \dot{\bar{v}}$) and their Poincaré maps of the steady-state response are shown representing red points (e) 1, (f) 2, and (g) 3 for Configuration 8, and red points (h) 1, (i) 2, and (j) 3 for Configuration 10. Phase subspaces' colors represent the color code used in the entire work. The non-maximum values in the OPDs are plotted in grayscale in (a) and (b).

Figure 20 presents the same analysis for Configurations 8 and 10, where the piezoelectric transducer dominates the energy conversion. These configurations represent the least favorable scenario for the HMEH, characterized by a very narrow bandwidth. This is further illustrated by the red points of maximum that are precisely concentrated at the resonance region of the \bar{z} -direction. It also supports the findings of figure 17(c), which shows a high occurrence percentage of

1T attractors in the regions of high performance above the $\bar{P}_{\text{norm}} \geq 0.3$ threshold. It is also important to highlight that the pendulum fully rotates around its axis (presents a high-amplitude motion) in only one selected red point of maximum.

In conclusion, this subsection effectively highlights the association of hyperchaotic responses and the full rotation of the pendulum with wider bandwidths and enhanced performance.

4. Conclusions

This work deals with an extensive numerical investigation of the HMEH. The HMEH is an evolution of the CPEH that offers multidirectional capabilities through the inclusion of a pendulum structure at the free end of the CPEH. To counteract the pendulum's role as a dynamical energy absorber, an additional electromagnetic transducer is attached to the base of the pendulum to harness its rotational energy. A reduced-order model is proposed to describe the main characteristics of the HMEH, and a normalization procedure is done to generalize the analysis.

A parametric analysis is conducted, focusing on two key structural parameters, Ω_s and Ω_ϕ , and two excitation parameters, γ and Ω . Ω_s represents the ratio between the natural frequencies of the beam structure, while Ω_ϕ represents the ratio between the linearized natural frequency of the pendulum element and the natural frequency in the piezoelectric polarized direction. Greater values of Ω_s represent wider beam widths (a stiffer direction perpendicular to the piezoelectric element), and vice versa, while greater values of Ω_ϕ represent pendulum elements with shorter lengths, and vice versa. γ represents the magnitude of external excitation, while Ω represents the frequency of external excitation.

The parametric analysis is based on a nonlinear dynamics perspective framework based on parameter-space diagrams developed to map and quantify important characteristics of the system. Initially, system dynamics is assessed considering a specific external source, revealing complex types of periodic, quasi-periodic and aperiodic dynamical responses. Many of these dynamical attractors are characterized by the pendulum rotation, the pendulum oscillation around its equilibrium position, or mixed patterns where both oscillation and rotation occur.

Furthermore, it is demonstrated that a small change in any of the chosen four parameters can result in a complete change in the harvester's performance characteristics. As a result, an extensive array of 25×10^6 time series simulations are performed and compared to determine the best and the worst combination of structural parameters in terms of energy harvesting performance. Results show that configurations with greater values of Ω_s combined with small values of Ω_ϕ results in better performances regarding the operational bandwidth of the HMEH. In other words, configurations using beams with larger widths and wider pendulum lengths perform better than configurations with the opposite characteristics.

Additionally, configurations that present the best performances in terms of bandwidth demonstrated that both transducers contribute significantly to the overall energy conversion, but with the predominance of the electromagnetic transducer. Moreover, configurations that present balanced levels of contributions in energy conversion by both transducers were demonstrated to have shorter bandwidths with greater levels of maximum output power. Alternatively, configurations that show the predominance of the piezoelectric transducer demonstrated tiny bandwidths comparable to those

presented by the CPEH in the literature. These configurations represent the worst-case scenario for the HMEH harvester.

Finally, a comparison among dynamical responses and patterns is carried out, showing that the majority of dynamical responses related to the overall higher performances are associated with hyperchaotic attractors with 68.5% of occurrence, followed by 1T attractors with 15.7% occurrence, and chaotic with 11.5% occurrence. 2T regular responses present a 3.1% of the total occurrences. Results suggest an association of larger operational bandwidths with the irregular dynamical pattern characterized by both oscillation and rotation of the pendulum (irregular mixed).

In conclusion, this work underscores the importance of an extensive numerical analysis based on a nonlinear dynamics perspective to understand important characteristics of an energy harvesting system. The analysis provided valuable insights into the structural characteristics of the HMEH to achieve higher performances in operational conditions that require multidirectional capabilities.

Data availability statement

The data that support the findings of this study are available from the corresponding author upon reasonable request.

Acknowledgments

The authors would like to acknowledge the support of the Brazilian Research Agencies CNPq (Conselho Nacional de Desenvolvimento Científico e Tecnológico) through grants 306.079/2023-2, 403.250/2023-4, and 441.460/2023-2; CAPES (Coordenação de Aperfeiçoamento de Pessoal de Nível Superior) - through grant 88881.974019/2024-01; FAPERJ (Fundação Carlos Chagas Filho de Amparo à Pesquisa do Estado do Rio de Janeiro) through grant E-26/201.017/2022. The authors also acknowledge support from the INCT-EIE (National Institute of Science and Technology - Smart Structures in Engineering), funded by CNPq, CAPES and FAPEMIG (Fundação de Amparo à Pesquisa do Estado de Minas Gerais), grant 406.148/2022-8; and the support of the AFOSR (Air Force Office of Scientific Research) through grant FA9550-23-4301-0527. Moreover, the authors also appreciate the use of the computational resources of the NACAD (Advanced High-Performance Computing Nucleus).

Appendix. Construction of 2D Diagrams

This appendix provides details of the method to construct diagrams utilized in the dynamical analysis of this work. All diagrams are built based on an array of successive numerical simulations of the dynamical system with different selected parameters. Given this intensive computational task, these numerical simulations are performed using the fourth-order Runge-Kutta scheme, considering a time step $\Delta\tau \propto 2\pi/\Omega$.

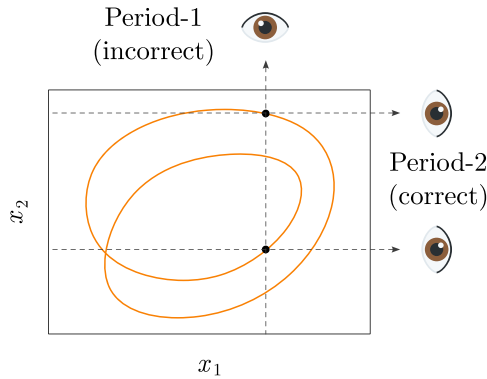


Figure A.1. Relying on the monitoring of a single state variable of the Poincaré map points can lead to erroneous attractor classification due to the alignment of points.

This approach allows for accurate qualitative observations allied with performance.

The DRDs, OPDs, and DPDs are built with a grid of $N_x \times N_y$ sample points, each of which is obtained from a time series integration from τ_0 to τ_f , considering a suitable integration time step. A time τ_{trans} is chosen to define that steady state is reached, assumed to be $\tau_{\text{trans}} = 0.815\tau_f$. Additionally, all the samples share the same initial conditions to standardize the analysis, being subjected to 800 external forcing periods, T.

A.1. Dynamical Response Diagrams (DRDs)

The DRDs can be used as a tool to map and quantify the dynamical attractors of the system resulting from a specific initial condition within a 2D parameter space of choice. From each numerical integration sample, a behavior is classified. All classifications are based on the Lyapunov exponent spectrum and the verification of the steady state Poincaré map. Initially, the first two Lyapunov exponents, λ_1 and λ_2 , are analyzed. The behavior is classified based on the values of these exponents in which three behaviors are analyzed (periodic, chaotic and hyperchaotic). A $\lambda_1 < 0$ characterized periodic motion, while $\lambda_1 > 0$ and $\lambda_2 < 0$ characterizes chaotic motion. If both $\lambda_1 > 0$ and $\lambda_2 > 0$, the response is classified as hyperchaotic. If the classification is chaotic or hyperchaotic, the classification procedure is over. Otherwise, if the classification is periodic ($\lambda_1 < 0$), the Poincaré map of the steady state time series sample is analyzed.

A list of values with all the points of the Poincaré map is loaded, and the last point is used as the reference. Then, the previous points are analyzed one by one until they find an equal at the i th position. After that, if it finds another equal value in the $2i$ th position, then it can be classified as a i -periodic candidate, if not, it continues to analyze previous points until these two conditions are met. The same procedure is done for all dimensions of the system, and the greatest periodic behavior found is used as the final classification. The comparison of all state variables is needed as

limiting the observation to only one direction may yield misleading results of smaller periodicity due to the alignment of points in this direction, as indicated in figure A.1. A tolerance of $p_{\text{tol}} = (x_{\max} - x_{\min})\mathcal{O}_{\text{method}}$ for each state variable must be placed when comparing the points, where x_{\max} and x_{\min} are the maximum and minimum values of the state variable between τ_{trans} and τ_f (steady state), and $\mathcal{O}_{\text{method}}$ is the order of error of the method of integration. The procedure depicting the comparison of the Poincaré map data is illustrated in figure A.2. Different periodicities are classified by colors as discussed in section 3. Regarding quasi-periodic behavior ($\lambda_1 = 0$), the algorithm considers it as a part of Many Periods classification (MP), as also discussed in section 3.

A.2. Average OPDs

These diagrams are constructed in a way that for all numerical integration samples within the two-dimensional parameter space, the steady-state output power is computed using the quantities presented in equation (26).

A.3. DPDs

The DPDs is an extension of the DRD that helps to identify distinct types of dynamical patterns unique to the analyzed dynamical system. In this case, it maps and identifies different patterns of rotation related to the pendulum. For each integration sample, it monitors the coordinate transformed state space of the pendulum $\bar{\phi} \times \dot{\bar{\phi}}$ and its associated dynamical attractor. The process of coordinate transformation of $\bar{\phi}$ is discussed in section 3.2, and it is done due to the phase subspace of the pendulum being characterized by a cylinder topology. Based on the minimum and maximum values of the angular position of the pendulum, $\bar{\phi}_{\min}$ and $\bar{\phi}_{\max}$, respectively, on the signal of the angular velocity $\dot{\bar{\phi}}$, and on the dynamical response classification of the DRD, it classified six different dynamical patterns as summarized in table A.1. Each classification is represented by a distinct color as presented in figure 16.

Poincaré Map Data

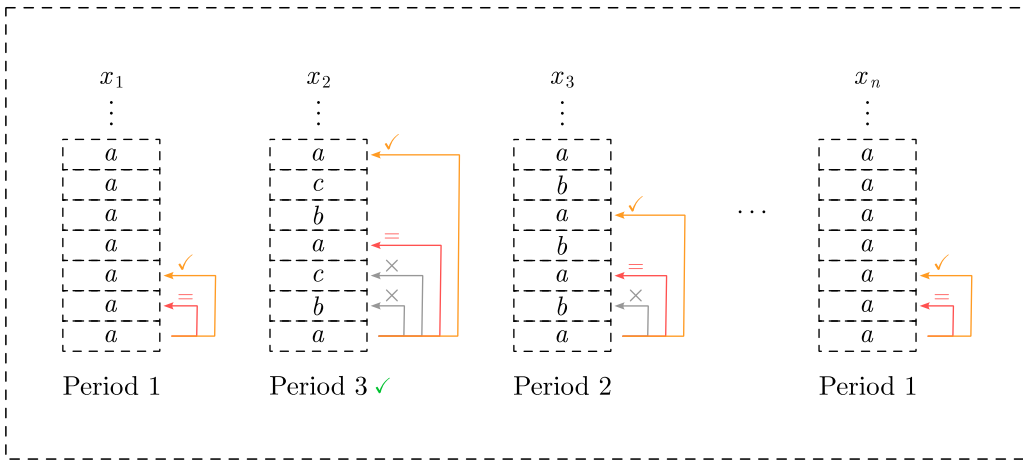


Figure A.2. Procedure to classify periodic attractors using Poincaré map data. a , b and c are arbitrary numbers to represent the real data. x_1, x_2, \dots, x_n represent the n state variables within the state space of the system. Light gray arrows followed by a ‘ \times ’ represent that the two values compared are not equal. Alternatively, red arrows labeled as ‘=’ represent positive equality in the comparison (i th position). Finally, the orange arrows labeled with a \checkmark represent the $2i$ th position at which the value is equal to the i th position. The greatest orange value is chosen as the final classification and, it is marked by the green checkmark.

Table A.1. Conditions for each dynamical pattern classification for the HMEH.

Dynamical Pattern Classification	Conditions
RO (Regular Oscillation)	<ul style="list-style-type: none"> • $\bar{\phi}_{\min} > -\pi$ and $\bar{\phi}_{\max} < \pi$ • $\text{sgn}(\dot{\phi}_{\min}) \neq \text{sgn}(\dot{\phi}_{\max})$ • Attractor \neq CH and Attractor \neq HC
IO (Irregular Oscillation)	<ul style="list-style-type: none"> • $\bar{\phi}_{\min} > -\pi$ and $\bar{\phi}_{\max} < \pi$ • $\text{sgn}(\dot{\phi}_{\min}) \neq \text{sgn}(\dot{\phi}_{\max})$ • Attractor = CH or Attractor = HC
RR (Regular Rotation)	<ul style="list-style-type: none"> • $\bar{\phi}_{\min} \leq -\pi$ and $\bar{\phi}_{\max} \geq \pi$ • $\text{sgn}(\dot{\phi}_{\min}) = \text{sgn}(\dot{\phi}_{\max})$ • Attractor \neq CH and Attractor \neq HC
IR (Irregular Rotation)	<ul style="list-style-type: none"> • $\bar{\phi}_{\min} \leq -\pi$ and $\bar{\phi}_{\max} \geq \pi$ • $\text{sgn}(\dot{\phi}_{\min}) = \text{sgn}(\dot{\phi}_{\max})$ • Attractor = CH or Attractor = HC
RM (Regular Mixed)	<ul style="list-style-type: none"> • $\bar{\phi}_{\min} \leq -\pi$ and $\bar{\phi}_{\max} \geq \pi$ • $\text{sgn}(\dot{\phi}_{\min}) \neq \text{sgn}(\dot{\phi}_{\max})$ • Attractor \neq CH and Attractor \neq HC
IM (Irregular Mixed)	<ul style="list-style-type: none"> • $\bar{\phi}_{\min} \leq -\pi$ and $\bar{\phi}_{\max} \geq \pi$ • $\text{sgn}(\dot{\phi}_{\min}) \neq \text{sgn}(\dot{\phi}_{\max})$ • Attractor = CH or Attractor = HC

A.4. OCDs

The procedure to construct an OCD involves the progressive analysis of different 2D diagram datasets. To illustrate this concept, consider a generic system characterized by three parameters: a , b and c . Within the parameter domain defined by $a \times b$, n distinct diagrams are generated, each representing a different value of the c parameter (c_1, c_2, \dots, c_n). Suppose the goal is to visually depict the prevalence of the *red characteristic* of the system and assess where, within the

$a \times b$ parameter domain, this characteristic is most prominent for a range of values of c .

To achieve this, all data points exhibiting the red characteristic are marked with the number 1, and all the remaining data points that do not exhibit the characteristic with the number 0. By summing up the values of each point in their respective locations within the parameter domain, the resulting dataset is produced. This dataset indicates how frequently the red feature appears at each unique point within the parameter domain. This procedure is illustrated in figure A.3.

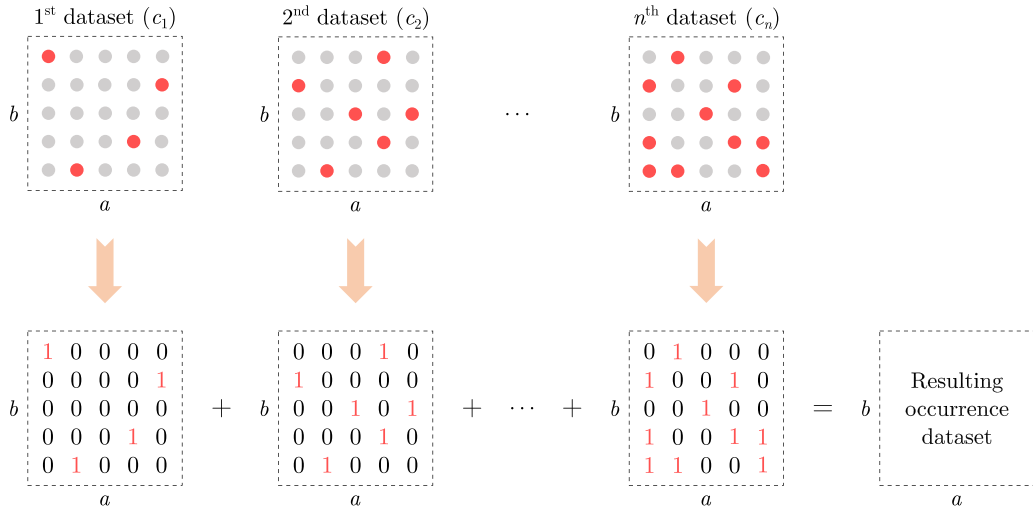


Figure A.3. Procedure to construct the occurrence diagrams (OCDs). Red points are related to the points that have the wanted characteristic, while gray points do not have the wanted characteristic. For each red point, the location within the diagram is marked as 1, while for each gray point, the location is marked as 0. The resulting occurrence dataset is the sum of all datasets.

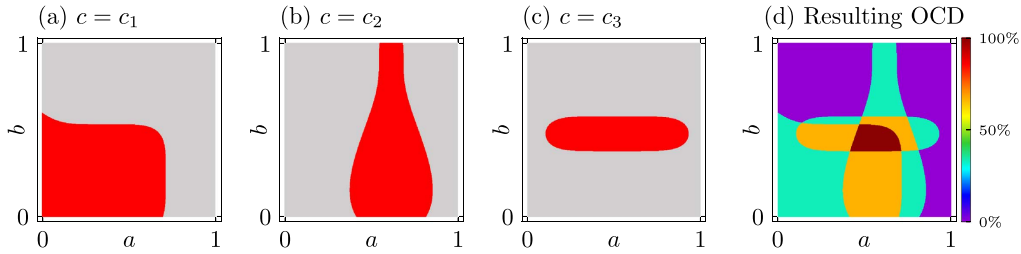


Figure A.4. In the first row are displayed 3 pseudo-random diagrams used to construct the resulting OCD in the second row. The colorbar in the second row represents the likelihood of the red characteristic to emerge within the $a \times b$ parameter space, based on the diagrams provided to construct the resulting OCD.

Moreover, 400 pseudo-random data were generated to simulate a data collection, to provide a comprehensive view of how the number of analyzed sample diagrams influences the resulting OCD. In figures A.4(a)–(c), 3 of these data collections are displayed in diagrams, which are used to construct the OCD. The resulting OCD, presented in figure A.4(d), indicates that the area within the parameter space $a \times b$ that the red characteristic is mostly likely to emerge is predominantly

centered at the intersection of the three red areas. This serves as a comprehensive illustration of the procedure outlined in figure A.3. By increasing the number of diagram samples to 400, as exemplified in figure A.5, the resulting OCD undergoes significant changes, displaying a notable shift in the region where the red characteristic is more likely to emerge. This result shows that the increase in available data to construct the OCD provides more accuracy in the predictions.

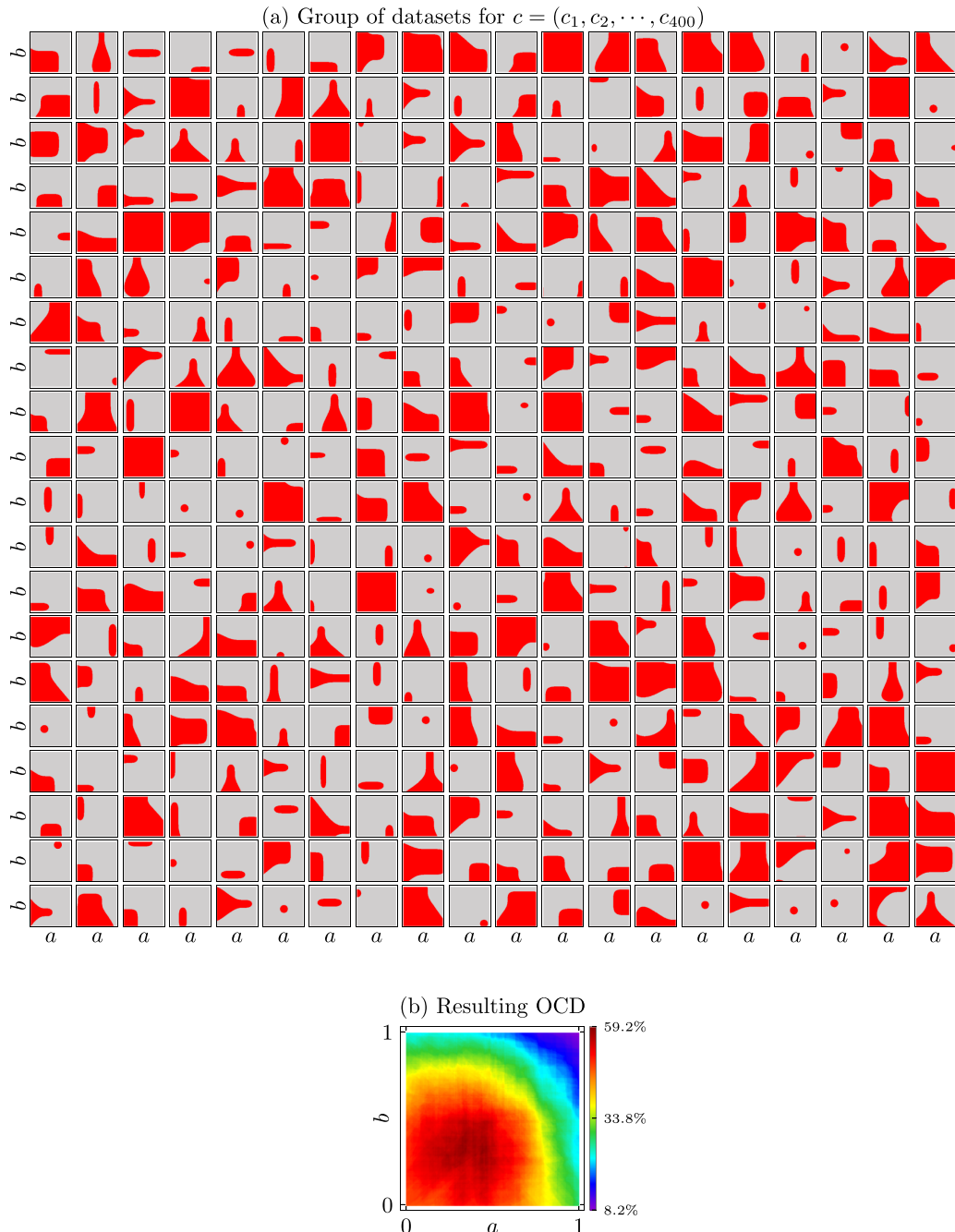


Figure A.5. 400 pseudo-random diagrams are displayed and used to construct the resulting OCD displayed at the bottom. The colorbar represents the likelihood of the red characteristic to emerge within the $a \times b$ parameter space, based on the diagrams provided to construct the resulting OCD.

ORCID iDs

Luã G Costa <https://orcid.org/0000-0002-2836-723X>
 Marcelo A Savi <https://orcid.org/0000-0001-5454-5995>

References

- Abdelkefi A, Najar F, Nayfeh A H and Ayed S B 2011 An energy harvester using piezoelectric cantilever beams undergoing coupled bending-torsion vibrations *Smart Mater. Struct.* **20** 115007
- Abdelmoula H, Sharpes N, Abdelkefi A, Lee H and Priya S 2017 Low-frequency zigzag energy harvesters operating in torsion-dominant mode *Appl. Energy* **204** 413–9
- Adeodato A, Duarte B T, Monteiro L L S, Pacheco P M C and Savi M A 2021 Synergistic use of piezoelectric and shape memory alloy elements for vibration-based energy harvesting *Int. J. Mech. Sci.* **194** 106206
- Ai R, Monteiro L L S, Monteiro P C C, Pacheco P M C L and Savi M A 2019 Piezoelectric vibration-based energy harvesting enhancement exploiting nonsmoothness *Actuators* **8** 1
- Bai Q, Gan C-Z, Zhou T, Du Z-C, Wang J-H, Wang Q, Wei K-X and Zou H-X 2024 A triboelectric-piezoelectric-electromagnetic

- hybrid wind energy harvester based on a snap-through bistable mechanism *Energy Convers. Manage.* **306** 118323
- Cabeza C, Briozzo C A, Garcia R, Freire J G, Marti A C and Gallas J A 2013 Periodicity hubs and wide spirals in a two-component autonomous electronic circuit *Chaos Solitons Fractals* **52** 59–65
- Caetano V J and Savi M A 2021 Multimodal pizza-shaped piezoelectric vibration-based energy harvesters *J. Intell. Mater. Syst. Struct.* **32** 2505–28
- Carvalho P R and Savi M A 2020 Synchronization and chimera state in a mechanical system *Nonlinear Dyn.* **102** 907–25
- Cepnik C, Lausecker R and Wallrabe U 2013 Review on electrodynamic energy harvesters-a classification approach *Micromachines* **4** 168–96
- Chen J, Bao B, Liu J, Wu Y and Wang Q 2022 Pendulum energy harvesters: a review *Energies* **15** 22
- Chen X, Zhang X, Chen L, Guo Y and Zhu F 2021a A curve-shaped beam bistable piezoelectric energy harvester with variable potential well: modeling and numerical simulation *Micromachines* **12** 8
- Chen X, Zhang X, Wang L and Chen L 2021b An arch-linear composed beam piezoelectric energy harvester with magnetic coupling: design, modeling and dynamic analysis *J. Sound Vib.* **513** 116394
- Chung J, Song M, Chung S-H, Choi W, Lee S, Lin Z-H, Hong J and Lee S 2021 Triangulated cylinder origami-based piezoelectric/triboelectric hybrid generator to harvest coupled axial and rotational motion *Research* **2021** 7248579
- Clementi G, Cottone F, Di Michele A, Gammaioni L, Mattarelli M, Perna G, López-Suárez M, Baglio S, Trigona C and Neri I 2022 Review on innovative piezoelectric materials for mechanical energy harvesting *Energies* **15** 17
- Costa L G, da Silva Monteiro L L, Pacheco P M C L and Savi M A 2021 A parametric analysis of the nonlinear dynamics of bistable vibration-based piezoelectric energy harvesters *J. Intell. Mater. Syst. Struct.* **32** 699–723
- Costa L G, Monteiro L L S and Savi M A 2024 Multistability investigation for improved performance in a compact nonlinear energy harvester *J. Braz. Soc. Mech. Sci. Eng.* **46** 212
- Costa L G and Savi M A 2024a Nonlinear dynamics of a compact and multistable mechanical energy harvester *Int. J. Mech. Sci.* **262** 108731
- Costa L G and Savi M A 2024b Pendulum-based hybrid system for multidirectional energy harvesting *Nonlinear Dyn.* **112** 18665–84
- Dagdeviren C et al 2014 Conformal piezoelectric energy harvesting and storage from motions of the heart, lung and diaphragm *Proc. Natl Acad. Sci.* **111** 1927–32
- De Paula A S, Inman D J and Savi M A 2015 Energy harvesting in a nonlinear piezomagnetoelastic beam subjected to random excitation *Mech. Syst. Signal Process.* **54–55** 405–16
- Delnavaz A and Voix J 2014 Flexible piezoelectric energy harvesting from jaw movements *Smart Mater. Struct.* **23** 105020
- Deng Z and Dapino M J 2017 Review of magnetostrictive vibration energy harvesters *Smart Mater. Struct.* **26** 103001
- Deterre M, Lefevre E and Dufour-Gergam E 2012 An active piezoelectric energy extraction method for pressure energy harvesting *Smart Mater. Struct.* **21** 085004
- Dutoit N E, Wardle B L and Kim S-G 2005 Design considerations for mems-scale piezoelectric mechanical vibration energy harvesters *Integr. Ferroelectr.* **71** 121–60
- Edge K-J I, Matin Nazar A and Jiao P 2022 Piezoelectric-triboelectric-electromagnetic hybrid rotational energy harvesters (H-REH) *Int. J. Mech. Sci.* **235** 107722
- Elhalwagy A M, Ghoneem M Y M and Elhadidi M 2017 Feasibility study for using piezoelectric energy harvesting floor in buildings' interior spaces *Energy Proc.* **115** 114–26
- Erturk A 2011 Piezoelectric energy harvesting for civil infrastructure system applications: moving loads and surface strain fluctuations *J. Intell. Mater. Syst. Struct.* **22** 1959–73
- Erturk A and Inman D 2011 Broadband piezoelectric power generation on high-energy orbits of the bistable duffing oscillator with electromechanical coupling *J. Sound Vib.* **330** 2339–53
- Fan K-Q, Chao F-B, Zhang J-G, Wang W-D and Che X-H 2014 Design and experimental verification of a bi-directional nonlinear piezoelectric energy harvester *Energy Convers. Manage.* **86** 561–7
- Gao L et al 2020 A self-powered and self-functional tracking system based on triboelectric-electromagnetic hybridized blue energy harvesting module *Nano Energy* **72** 104684
- Gao S, Zhang G, Jin L, Li P and Liu H 2017 Study on characteristics of the piezoelectric energy-harvesting from the torsional vibration of thin-walled cantilever beams *Microsyst. Technol.* **23** 5455–65
- Halim M A, Kabir M H, Cho H and Park J Y 2019 A frequency up-converted hybrid energy harvester using transverse impact-driven piezoelectric bimorph for human-limb motion *Micromachines* **10** 10
- Haroun A, Tarek M, Mosleh M and Ismail F 2022 Recent progress on triboelectric nanogenerators for vibration energy harvesting and vibration sensing *Nanomaterials* **12** 17
- Hu G, Liang J, Lan C and Tang L 2020 A twist piezoelectric beam for multi-directional energy harvesting *Smart Mater. Struct.* **29** 11LT01
- Izadgoshasb I 2021 Piezoelectric energy harvesting towards self-powered internet of things (iot) sensors in smart cities *Sensors* **21** 24
- Jia J, Shan X, Upadrashta D, Xie T, Yang Y and Song R 2020 An asymmetric bending-torsional piezoelectric energy harvester at low wind speed *Energy* **198** 117287
- Kumar R, Gupta S and Ali S F 2019 Energy harvesting from chaos in base excited double pendulum *Mech. Syst. Signal Process.* **124** 49–64
- Lee J and Choi B 2014 Development of a piezoelectric energy harvesting system for implementing wireless sensors on the tires *Energy Convers. Manage.* **78** 32–38
- Li H, Liu D, Wang J, Shang X and Hajj M R 2020 Broadband bimorph piezoelectric energy harvesting by exploiting bending-torsion of l-shaped structure *Energy Convers. Manage.* **206** 112503
- Li H, Lu J, Myjak M J, Liss S A, Brown R S, Tian C and Deng Z D 2022 An implantable biomechanical energy harvester for animal monitoring devices *Nano Energy* **98** 107290
- Liu H, Lee C, Kobayashi T, Tay C J and Quan C 2012 Investigation of a mems piezoelectric energy harvester system with a frequency-widened-bandwidth mechanism introduced by mechanical stoppers *Smart Mater. Struct.* **21** 035005
- Liu Y, Khanbareh H, Halim M A, Feeney A, Zhang X, Heidari H and Ghannam R 2021 Piezoelectric energy harvesting for self-powered wearable upper limb applications *Nano Select* **2** 1459–79
- Malaji P V, Friswell M I, Adhikari S and Litak G 2020 Enhancement of harvesting capability of coupled nonlinear energy harvesters through high energy orbits *AIP Adv.* **10** 085315
- Margielewicz J, Gaska D, Litak G, Wolszczak P and Yurchenko D 2022 Nonlinear dynamics of a new energy harvesting system with quasi-zero stiffness *Appl. Energy* **307** 118159
- Margielewicz J, Gaska D, Litak G, Yurchenko D, Wolszczak P, Dymarek A and Dzitkowski T 2023 Influence of the configuration of elastic and dissipative elements on the energy harvesting efficiency of a tunnel effect energy harvester *Chaos Solitons Fractals* **167** 113060
- Masana R and Daqaq M F 2010 Electromechanical modeling and nonlinear analysis of axially loaded energy harvesters *J. Vib. Acoust.* **133** 1

- Meirovitch L 2010 *Methods of Analytical Dynamics (Advanced Engineering Series)* (Dover Publications)
- Nabavi S F, Farshidianfar A and Afsharfard A 2018 Novel piezoelectric-based ocean wave energy harvesting from offshore buoys *Appl. Ocean Res.* **76** 174–83
- Pan J-N, Qin W-Y, Deng W-Z and Zhou H-L 2019 Harvesting base vibration energy by a piezoelectric inverted beam with pendulum* *Chin. Phys. B* **28** 017701
- Pan J, Qin W, Deng W, Zhang P and Zhou Z 2021 Harvesting weak vibration energy by integrating piezoelectric inverted beam and pendulum *Energy* **227** 120374
- Peigney M and Siegert D 2013 Piezoelectric energy harvesting from traffic-induced bridge vibrations *Smart Mater. Struct.* **22** 095019
- Preumont A 2006 *Mechatronics: Dynamics of Electromechanical and Piezoelectric Systems* (Springer)
- Reis E V and Savi M A 2022 Spatiotemporal chaos in a conservative duffing-type system *Chaos Solitons Fractals* **165** 112776
- Savi M A 2017 *Dinamica Nao-Linear e Caos* 2 edn (E-papers)
- Savi P V and Savi M A 2024 Nonlinear dynamics of an adaptive energy harvester with magnetic interactions and magnetostrictive transduction *Smart Struct. Syst.* **33** 281–90
- Sebald G, Tung N T, Taxil G, Ducharme B, Chavez J, Ono T, Kuwano H, Lefevre E and Lallart M 2023 Piezoelectric small scale generator: towards near-joule output energy generation *Smart Mater. Struct.* **32** 085009
- Stanton S C, McGehee C C and Mann B P 2009 Reversible hysteresis for broadband magnetopiezoelectric energy harvesting *Appl. Phys. Lett.* **95** 174103
- Su W-J and Zu J 2013 An innovative tri-directional broadband piezoelectric energy harvester *Appl. Phys. Lett.* **103** 203901
- Tavares R and Ruderman M 2020 Energy harvesting using piezoelectric transducers for suspension systems *Mechatronics* **65** 102294
- Toprak A and Tigli O 2014 Piezoelectric energy harvesting: State-of-the-art and challenges *Appl. Phys. Rev.* **1** 031104
- Tripathy A, Saravanakumar B, Mohanty S, Nayak S K and Ramadoss A 2021 Comprehensive review on flexoelectric energy harvesting technology: mechanisms, device configurations and potential applications *ACS Appl. Electr. Mater.* **3** 2898–924
- Wang C, Ji Y, Lai S-K, Liu Y, Hao Y, Li G, Wang C and Wen G-L 2023 A speed-amplified tri-stable piezoelectric-electromagnetic-triboelectric hybrid energy harvester for low-frequency applications *Nano Energy* **114** 108630
- Wang C, Zhao J, Li Q and Li Y 2018 Optimization design and experimental investigation of piezoelectric energy harvesting devices for pavement *Appl. Energy* **229** 18–30
- Wang T 2023 Pendulum-based vibration energy harvesting: mechanisms, transducer integration and applications *Energy Convers. Manage.* **276** 116469
- Wang Y, Zhao Y, Chen C, Cao D and Yang Z 2022a Misalignment-induced bending-torsional coupling vibrations of doubly-clamped nonlinear piezoelectric energy harvesters *Mech. Syst. Signal Process.* **169** 108776
- Wang Z, Du Y, Li T, Yan Z and Tan T 2022b Bioinspired omnidirectional piezoelectric energy harvester with autonomous direction regulation by hovering vibrational stabilization *Energy Convers. Manage.* **261** 115638
- Williams C and Yates R 1996 Analysis of a micro-electric generator for microsystems *Sensors Actuators A* **52** 8–11
- Wu H, Tang L, Yang Y and Soh C K 2013 A novel two-degrees-of-freedom piezoelectric energy harvester *J. Intell. Mater. Syst. Struct.* **24** 357–68
- Wu H, Tang L, Yang Y and Soh C K 2014 Development of a broadband nonlinear two-degree-of-freedom piezoelectric energy harvester *J. Intell. Mater. Syst. Struct.* **25** 1875–89
- Wu Y, Li S, Fan K, Ji H and Qiu J 2022 Investigation of an ultra-low frequency piezoelectric energy harvester with high frequency up-conversion factor caused by internal resonance mechanism *Mech. Syst. Signal Process.* **162** 108038
- Wu Y, Qiu J, Zhou S, Ji H, Chen Y and Li S 2018 A piezoelectric spring pendulum oscillator used for multi-directional and ultra-low frequency vibration energy harvesting *Appl. Energy* **231** 600–14
- Xiao Y, Nie M, Yang L, Liu J, Lv X and Yang P 2022 Integrated triboelectric-electromagnetic-piezoelectric self-rebounding energy harvester for human energy harvesting *Adv. Mater. Technol.* **7** 2200340
- Xu J and Tang J 2015 Multi-directional energy harvesting by piezoelectric cantilever-pendulum with internal resonance *Appl. Phys. Lett.* **107** 213902
- Yang T and Cao Q 2019 Dynamics and performance evaluation of a novel tristable hybrid energy harvester for ultra-low level vibration resources *Int. J. Mech. Sci.* **156** 123–36
- Yang Z, Wang Y Q, Zuo L and Zu J 2017 Introducing arc-shaped piezoelectric elements into energy harvesters *Energy Convers. Manage.* **148** 260–6
- Yuan J H, Yang Y Z and Zhang Y H 2019 A piezoelectric energy harvester with light-activated shape memory polymers *Ferroelectrics* **550** 98–111
- Zhang X, Yang W, Zuo M, Tan H, Fan H, Mao Q and Wan X 2018 An arc-shaped piezoelectric bistable vibration energy harvester: modeling and experiments *Sensors* **18** 4472
- Zhao L-C, Zou H-X, Gao Q-H, Yan G, Liu F-R, Tan T, Wei K-X and Zhang W-M 2019 Magnetically modulated orbit for human motion energy harvesting *Appl. Phys. Lett.* **115** 263902
- Zhong X, Yang Y, Wang X and Wang Z L 2015 Rotating-disk-based hybridized electromagnetic-triboelectric nanogenerator for scavenging biomechanical energy as a mobile power source *Nano Energy* **13** 771–80
- Zhou S, Cao J, Inman D J, Liu S, Wang W and Lin J 2015 Impact-induced high-energy orbits of nonlinear energy harvesters *Appl. Phys. Lett.* **106** 093901
- Zhu J, Liu X, Shi Q, He T, Sun Z, Guo X, Liu W, Sulaiman O B, Dong B and Lee C 2020 Development trends and perspectives of future sensors and MEMS/NEMS *Micromachines* **11** 7
- Zuo L and Tang X 2013 Large-scale vibration energy harvesting *J. Intell. Mater. Syst. Struct.* **24** 1405–30